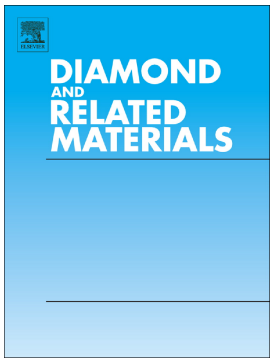
Journal Pre-proof



Engineering graphene quantum dots via laser ablation for epinephrine sensing

Philipi Cavalcante Ricardo, Caio Raphael Vanoni, Jorge Padrão, Andrea Zille, Veronica Satulu, Bogdana Mitu, Mario Rui da Cunha Pereira, Cristiane Luisa Jost, Filipe Samuel Silva, Marcio Celso Fredel

PII: S0925-9635(25)01150-1

DOI: https://doi.org/10.1016/j.diamond.2025.113093

Reference: DIAMAT 113093

To appear in: *Diamond & Related Materials*

Received date: 15 September 2025

Revised date: 30 October 2025

Accepted date: 15 November 2025

Please cite this article as: P.C. Ricardo, C.R. Vanoni, J. Padrão, et al., Engineering graphene quantum dots via laser ablation for epinephrine sensing, *Diamond & Related Materials* (2024), https://doi.org/10.1016/j.diamond.2025.113093

This is a PDF of an article that has undergone enhancements after acceptance, such as the addition of a cover page and metadata, and formatting for readability. This version will undergo additional copyediting, typesetting and review before it is published in its final form. As such, this version is no longer the Accepted Manuscript, but it is not yet the definitive Version of Record; we are providing this early version to give early visibility of the article. Please note that Elsevier's sharing policy for the Published Journal Article applies to this version, see: https://www.elsevier.com/about/policies-and-standards/sharing#4-published-journal-article. Please also note that, during the production process, errors may be discovered which could affect the content, and all legal disclaimers that apply to the journal pertain.

© 2025 Published by Elsevier B.V.

Journal Pre-proof

Engineering Graphene Quantum Dots via Laser Ablation for Epinephrine Sensing

Philipi Cavalcante Ricardo[a], Caio Raphael Vanoni[b], Jorge Padrão[c], Andrea Zille[c], Veronica Satulu[d], Bogdana Mitu[d], Mario Rui da Cunha Pereira[e], Cristiane Luisa Jost[b], Filipe Samuel Silva[f], Marcio Celso Fredel[a*]

a Ceramic and Composite Materials Research Group (CERMAT), Mechanical Engineering Department, Federal University of Santa Catarina, Florianópolis, SC, Brazil

b ampere - Laboratório de Plataformas Eletroquímicas, Department of Chemistry, Federal University of Santa Catarina, Florianópolis, SC, 88040-900, Brazil

c Centre for Textile Science and Technology (2C2T), University of Minho, 4800-058 Guimarães, Portugal

d National Institute for Laser, Plasma and Radiation Physics, 409 Atomistilor Str., 077125, Magurele, Romania

e Centre of Physics of Minho and Porto Universities (CF-UM-UP), University of Minho, Campus de Gualtar, 4710-057 Braga, Portugal

f Center for MicroElectroMechanical Systems (CMEMS-UMinho), University of Minho, Guimarães, Portugal

*Corresponding author:

e-mail address: m.fredel@ufsc.br

Journal Pre-proof

Journal Pre-proof

ABSTRACT

In this study, we report a sustainable strategy for the synthesis of functionalized graphene quantum dots (GQDs) via pulsed laser ablation in liquid (PLAL), employing sodium-based salts (NaCl, $NaNO_3$, and Na_2SO_3) as functional sources to introduce chlorine, nitrogen, and sulfur, respectively. This single-step green synthesis yields highly pure GQDs with tunable optical and electrochemical properties. Comprehensive physicochemical characterization, including high-resolution transmission electron microscopy (HRTEM), Fourier transform infrared spectroscopy (FTIR), UV–Vis spectroscopy, photoluminescence (PL) spectroscopy, and X-ray photoelectron spectroscopy (XPS), confirmed controlled particle size distribution, successful surface functionalization, and distinct optoelectronic behavior. The GQDs were incorporated into Nafion®-modified glassy carbon electrodes (GCE) to fabricate electrochemical sensors for epinephrine (EP) detection. Among the GQDs, sulfur-functionalized samples exhibited superior sensitivity due to enhanced surface charge, improved electron transfer kinetics, and favorable interactions with the Nafion® matrix. The resulting sensor demonstrated a wide linear dynamic range (0.1–10 μM) and a low detection limit (LOD = 77 nM), underscoring its potential for pharmaceutical quality control. These findings demonstrate that salt-assisted PLAL can tune surface chemistry and may be extended for broader sensing applications.

Keywords: Pulsed laser ablation, green synthesis, voltammetry, electrochemical sensor, neurotransmitter.

Journal Pre-proof

1. INTRODUCTION

Graphene quantum dots (GQDs) are a class of zero-dimensional carbon nanomaterials, typically under 10 nm in lateral size, that exhibit pronounced quantum confinement and edge effects [1]. Their unique combination of tunable band gap, strong photoluminescence [2], high specific surface area, and outstanding charge-carrier mobility has stimulated intensive research across diverse fields [3]. Unlike many other fluorescent nanocrystals, GQDs can be derived in bulk from inexpensive, environmentally benign carbon feedstocks, ranging from graphite powder[4] and coal [5] to biomass [6] residues, without introducing hazardous heavy metals. Their inherently low density, chemical stability in aqueous and organic media, and responsiveness to surface functionalization make them particularly attractive for biological imaging [7], targeted drug delivery [8], light-emitting diodes (LEDs) [9], solar cells [10], and a new generation of electrochemical [11] and optical [12] sensors.

The production of graphene quantum dots may be achieved by two main approaches. Top-down techniques begin with layered carbon allotropes, such as graphene oxide, multi-walled carbon nanotubes, carbon fibers, or soot, and employ physical or chemical routes (e.g., ultrasonic exfoliation, chemical oxidation, laser ablation) to cleave these bulk materials into nanoscale fragments [13–15]. Parameters such as oxidant concentration, sonication power, laser fluence, or etching time can be tuned to control size, shape, and surface functional groups. In contrast, bottom-up approaches assemble GQDs atom-by-atom or molecule-by-molecule, often using small molecular precursors (citric acid, glucose, benzene derivatives, or fullerenes) under hydrothermal, solvothermal, or microwave-assisted conditions [16–18]. By adjusting reaction temperature (typically 120–200 °C), pressure (1–5 bar), reaction time, and precursor ratios, researchers can steer the formation of the characteristic honeycomb lattice and engineer emission wavelengths from the ultraviolet to the near-infrared. Recent advances also include heteroatom

doping (e.g., nitrogen, sulfur, phosphorus) to modulate electronic structure, and post-synthetic passivation strategies to improve quantum yield [19], photostability [20], and biocompatibility [21].

Doped GQDs are typically synthesized through a one-step hydrothermal or solvothermal process, where carbon precursors such as citric acid, glucose, or polyethylene glycol react with dopant agents at elevated temperatures between 120 and 200 °C under autogenous pressure [22,23]. Common heteroatom dopants include nitrogen, sulfur, phosphorus, and boron [23]. Nitrogen doping could involve the use of urea or ammonia [24], sulfur doping is often obtained by using thiourea [25] or sodium sulfate (Na_2SO_4)[26], phosphorus doping employs the utilization of sodium phytate [26], while boron can be added using boric acid [19]. During synthesis, dopants can be integrated into the graphitic core [27], at the edges [28], or within the defects [29] of the graphene structure, each affecting the characteristics of the GQDs differently. These modifications adjust the electronic structure by narrowing the band gap [30], and introducing additional redox-active sites [31]. As a result, doped GQDs demonstrate enhanced electrical conductivity, improved charge transfer kinetics, and superior electrocatalytic performance [32,33]. In electrochemical sensing, these properties lead to lower overpotentials, sharper redox peaks, and greater sensitivity and selectivity for analytes such as heavy metal ions, environmental contaminants, as well as biological-related ones, such as glucose or dopamine [34]. This makes doped GQDs a promising material for next-generation biosensors and environmental monitoring devices.

Pulsed laser ablation in liquid (PLAL) has gained attention as an effective and adaptable method for synthesizing GQDs, particularly within the framework of environmentally conscious nanotechnology [35]. Unlike conventional chemical synthesis routes, PLAL is based solely on physical interactions, which eliminates the necessity of large quantities of chemical precursors

and contributes to a reduced ecological footprint[36]. Owing to its use of ultrapure solvents and the absence of secondary chemical waste, the method avoids toxic acids, metal catalysts, and other hazardous reagents typical of hydrothermal or oxidative routes, ensuring high environmental safety and biocompatibility of the resulting GQDs [37]. The process typically involves directing high-intensity laser pulses onto a solid graphite target or dispersed graphite particles within a liquid, leading to plasma generation and subsequent particle formation as the plasma rapidly cools[38]. A notable advantage of PLAL is its ability to proceed under ambient conditions, without the need for extreme temperatures or pressures, which enhances both its practicality and energy efficiency. Furthermore, this technique enables the production of nanomaterials with high structural and chemical purity, as the absence of reactive or corrosive chemicals limits contamination risks and the formation of undesired by-products [39,40]. From a sustainability perspective, PLAL technique aligns with several United Nations Sustainable Development Goals (SDGs), including SDG 9 (Industry, Innovation and Infrastructure) [40], SDG 12 (Responsible Consumption and Production) [41], and SDG 13 (Climate Action) [42]. Its clean, energy-efficient nature and minimal reliance on hazardous substances position PLAL as a forward-thinking strategy for advancing green nanotechnology and sustainable materials development.

Epinephrine (EP), also known as adrenaline, is a key catecholamine neurotransmitter and hormone that coordinates both central and peripheral stress responses as well as cardiovascular homeostasis [43,44]. Under basal conditions, circulating EP levels reside in the low nanomolar range, yet acute physical or psychological stress can amplify their concentration by an order of magnitude, or even up to fifty-fold, through sympathoadrenal activation, thereby ensuring rapid mobilization of glucose and oxygen to vital organs and skeletal muscles [45,46]. Clinically, EP is also administered to manage critical conditions such as cardiac arrest, septic

Journal Pre-proof

shock, acute hypertension, bronchospasm in asthma, and anaphylaxis [47]. Given that deviations from physiological EP levels are implicated in a spectrum of disorders, trace-level measurement of EP in biological fluids is of crucial importance for both diagnostics and therapeutic monitoring [48]. To this end, an array of analytical approaches has been investigated, ranging from spectroscopic methods as UV-Vis, fluorescence [49], infrared, and chromatographic separations to capillary electrophoresis, colorimetric assays, chemiluminescence, and Surface-Enhanced Raman Scattering [49–54]. However, many of these techniques suffer from drawbacks such as insufficient sensitivity at ultralow concentrations, lengthy analysis periods, complex sample preparation protocols, high capital and operational costs, and reliance on environmentally hazardous solvents [48]. In contrast, according to the inherent redox activity of EP, its characteristic offers a promising direction for the design of electrochemical sensors that can deliver rapid, highly sensitive, and selective detection while mitigating environmental impact and simplifying the assay workflows [55].

To the best of our knowledge, despite growing interest in GQDs usage for electrochemical sensing, conventional synthesis methods such as hydrothermal, chemical oxidation, and solvothermal routes remain burdened by complex reaction schemes, hazardous reagents, environmental toxicity, and poor scalability. Under these circumstances, PLAL has emerged as an environmentally friendly, one-step, and solvent-free route for GQDs production. While several studies have employed salt-assisted PLAL for heteroatom incorporation, systematic comparison of different sodium salts under controlled conditions for tuning electrochemical performance remains limited. In this study, we introduce NaCl, $NaNO_3$, and Na_2SO_3 during PLAL process in order to incorporate chloride, nitrogen, and sulfur functionalities into GQDs, aiming to improve their electron transfer kinetics and stability. This approach eliminates corrosive reagents and reduces processing steps relative to hydrothermal methods.

Furthermore, the resulting GQDs offer enhanced sensitivity, selectivity, and operational stability for epinephrine detection, representing a cost-effective platform for advanced electrochemical sensing.

Journal Pre-proof

2. METHODS/EXPERIMENTAL

Chemicals. Sodium chloride, sodium nitrate, sodium sulfite, and ethyl alcohol (analytical grade, ≥ 99.5%) were purchased from Sigma-Aldrich. Carbon black (Vulcan XC72R) was donated by Cabot Corporation. All salts were dissolved in ultrapure water (resistivity ca. 18.2 MΩ·cm) obtained from a Milli-Q system (Millipore, Bedford, USA) to prepare the respective saline solutions used in the experiments. Nafion® (Sigma-Aldrich, 5%) was used for the modification of electrodes for cyclic voltammetry, while L-Epinephrine (Sigma-Aldrich, ≥ 99%) was employed to evaluate the sensor properties. The B-R buffer solutions were prepared from boric acid H_3BO_3 (Vetec, ≥ 99.5%, analytical grade), acetic acid CH_3COOH (Vetec, 95%), and phosphoric acid H_3PO_4 (Vetec, 95%). Solutions of hexaminеruthenium(III) chloride $[Ru(NH_3)_6]Cl_3$ and hexaammineruthenium(II) chloride $[Ru(NH_3)_6]Cl_2$ (Sigma-Aldrich, > 99%) at 1 mmol L^{-1} were used as redox probes for electrochemical measurements.

Preparation of Graphene Quantum Dots. GQDs suspensions were synthesized via pulsed laser ablation of a carbon black suspension at 1 mg mL^{-1} in ethyl alcohol (99.5% v/v) placed in a glass vessel containing 10 mL of the ethyl alcohol solution, by using a pulsed Nd:YAG laser (OEM Plus, Italy) fundamental wavelength of 1064 nm. The laser was operated at an output power of 3.3 W, with a spot size of 3 μm, a pulse width of 35 ns, and a repetition rate of 20 kHz. The laser beam was focused on the carbon surface suspension using a fused quartz lens with a focal length of 160 mm. Throughout the ablation process, continuous stirring was employed to ensure the homogeneous distribution of the carbon particles and to prevent decantation.

The non-functionalized GQDs were prepared using only carbon black and ethyl alcohol. For their functionalized variants, the respective salt precursors were dissolved in the ethanol medium to synthesize functionalized variants to achieve a final concentration of 1 mmol L^{-1} in the PLAL medium. Sodium chloride (NaCl) was used for the preparation of chlorine-GQDs (Cl-GQDs),

sodium nitrate ($NaNO_3$) for nitrogen-GQDs (N-GQDs), and sodium sulfite (Na_2SO_3) for sulfur-GQDs (S-GQDs). The duration of the ablation process was consistently set to 2 hours for all experiments. Following ablation, the resulting yellow-orange solution was filtered through a 220 nm syringe filter and stored in a refrigerator until further characterization.

UV−Vis Absorption Spectroscopy. UV–Vis spectra were recorded using a Shimadzu UV−1800 spectrophotometer (Shimadzu, Kyoto, Japan). Measurements were conducted in a 10 mm pathlength quartz cell with a sample volume of 2 mL, covering a spectral range from 190 to 800 nm.

Photoluminescence Spectroscopy. Photoluminescence (PL) spectroscopy was performed in a bench spectrofluorometer (F-7000 FL Spectrophotometer). The excitation and emission wavelengths were recorded in the 200–500 nm and 210–700 nm ranges, respectively, with increments of 10 nm. Excitation and emission slits were set at 5 nm. A quartz cuvette with a 1 cm optical pathlength and four polished faces was used. Measurements were taken using a 90° geometry configuration between the excitation and emission beams.

Fluorescent Lifetime Decay. Fluorescence lifetime measurements were carried out using a time-correlated single-photon counting (TCSPC) system incorporating a NanoLed® light source (Horiba, Jovin-Yvon, IBH Ltd.) emitting at 370 nm, with a pulse repetition frequency of 1 MHz. The excitation wavelength was selected via a monochromator, while fluorescence emission was isolated using optical filters and detected by a Hamamatsu R2949 photomultiplier tube. Signal acquisition was performed using a Becker & Hickl SPC-150 TCSPC module, and the resulting data were analyzed using the FluoFit software package from PicoQuant [56]. Fluorescence decay profiles were fitted using a multi-exponential decay model:

$$I(t) = \sum_i^n \alpha_i \exp(-\frac{t}{\tau_i}) \quad (1)$$

Journal Pre-proof

where *I(t)* represent the time-dependent fluorescence intensity, α_i denotes the amplitude, and τ_i corresponds to the fluorescence lifetime for each decay component. The quality of the fit was evaluated based on the chi-squared (χ^2) value and analysis of the residuals and their autocorrelation. The contribution of each decay component to the overall fluorescence, denoted as f_i, was subsequently calculated using the fractional intensity equation (2) [56].

$$f_i = \frac{\alpha_i \tau_i}{\sum_j^n \alpha_i \tau_i} \quad (2)$$

ATR-FTIR. Attenuated Total Reflectance Fourier Transform Infrared (ATR-FTIR) spectra were recorded using a PerkinElmer Spectrum 100 FT-IR in the range from 4000 to 600 cm^{-1}. To collect each spectrum, a small powder amount (3 mg) of each sample was analyzed by using ATR module equipped with a diamond/ZnSe crystal. Each spectrum was collected using 64 scans and a resolution of 1 cm^{-1}.

High-Resolution Transmission Electron Microscopy (HRTEM). HRTEM analyses were conducted using a Hitachi HD-2700 aberration-corrected STEM operated at 200 kV. Sample preparation involved drop-casting 10 μL of the colloidal solutions onto carbon-coated copper grids, followed by air drying.

X-Ray Photoelectron Spectroscopy (XPS). XPS measurements were carried out using a Thermo Scientific K-Alpha spectrometer (ESCALAB™ XI+), equipped with a monochromatic Al Kα radiation source (hv = 1486.6 eV), a 400 μm beam spot, and a double-focusing hemispherical analyzer. Analyses were performed under ultrahigh vacuum conditions ($<10^{-8}$ mbar), with charge compensation achieved using a flood gun. For each sample, survey spectra were collected over 10 scans using a pass energy of 200 eV, a step size of 1 eV, and a dwell time of 10 ms. High-resolution spectra for C1s, O1s, Na1s, N1s, Cl2p, and S2p were also acquired in 10 scans, using a lower pass energy of 20 eV, a finer step size of 0.025 eV, and an extended

dwell time of 100 ms. The C1s peak of adventitious carbon at 284.8 eV was served as the reference for energy calibration. Spectral deconvolution and oxidation states fitting were performed using Thermo Advantage software (version 5.9921), applying a Shirley background correction and a Gaussian-Lorentzian (GL (30)) peak shape.

Laser interferometry. The laser interferometry was performed using a contactless, three-dimensional, and scanning green light interferometer by Zygo ZeGage™ equipment with an optical resolution from 0.52 to 9.50 µm. The sample was prepared by drop coating 15 µL of Nafion® 0.15 % on the surface of a precleaned GCE (Ø = 3 mm) and letting it dry in the oven at 60 °C for 5 minutes. The sample was positioned in the equipment with 10x magnification and the acquired data were obtained and mathematically treated in ZYGO's Mx™ software.

Electrochemical measurements. The measurements were carried out with the potentiostat µStat-I 400s Methrom DropSens (Oviedo, Spain) and controlled by a PC with DropView 800 software for all the electrochemical studies. The setup containing three electrodes, such as GCE (Ø = 3 mm) as the working electrode, $Ag/AgCl/KCl_{(sat.)}$ as the reference electrode, and a platinum wire as the counter electrode, was used for electrochemical analyses. All the measurements were carried out in the electrolytic cell with a volume of 10 mL at room temperature. For each scan, the peak height was measured to assess the current intensity.

The GCE surface was carefully polished with alumina beads (0.3 and 0.05 µm), washed with distilled water, and sonicated with an ethanol/water solution for 15 minutes. For the electrode modification, eight solution systems were prepared with Nafion® and GQDs to reach 0.15% and 10 µg mL^{-1}, respectively, each with a volume of 1000 µL. The GQDs/Nafion® solutions were dispersed by ultrasonic for 30 minutes at room temperature. Subsequently, the GCE was modified with 15 µL of the corresponding system using the drop-coating method and then placed

into the oven at 60 °C for 5 minutes for complete solvent evaporation. The same procedure was repeated for each modification.

The sensors were characterized using a 1 mmol L^{-1} solution of hexamineruthenium (III) chloride $[Ru(NH_3)_6]Cl_3$ and hexaammineruthenium (II) chloride $[Ru(NH_3)_6]Cl_2$ with a 0.1 mol L^{-1} KCl solution. CV was applied over a potential range from + 0.2 V to − 0.6 V (*vs*. Ag/AgCl/$KCl_{(sat)}$) by using a scan rate (ν) of 50 mV. EIS measurements were made by – 0.15 V as VRef, 10 mV (rms) as Eamp, in a frequency range of 100 kHz to 0.1 Hz with 100 points.

The pH-related studies were conducted at values from 2.0 to 8.0, and the effect of the scan rate was carried out from 25 to 150 mV s^{-1} to evaluate electrochemical processes and mechanisms. The determination of EP was performed using cyclic voltammetry (CV) under a 50 mV s^{-1} scan rate. Finally, the values of the resulting current were used to construct the calibration curve with successive additions of aliquots of EP (n=3).

3. RESULTS AND DISCUSSION

3.1 Morphology and Yield

HRTEM was employed to characterize the structural features and spatial arrangement of GQDs, representative TEM micrographs (**Figure 1a-d**) of GQDs synthesized via PLAL exhibit a spherical morphology. A particle size distribution analysis was performed by statistically evaluating over 100 nanoparticles using ImageJ software. The resulting histograms fitted to a Normal function, except the Cl-GQDs system fitted with a Lognormal function (**Figure 1b**), indicate diameters ranging from 2.0 to 7.5 nm, with a mean size of 4.0 ± 0.8 nm for pure GQDs and 3.6 ± 0.5 nm for S-GQDs, the smallest system. These dimensions align with previously reported values for GQDs synthesized under analogous conditions [35,57,58], corroborating the reproducibility of the PLAL method in nanomaterial fabrication.

Journal Pre-proof

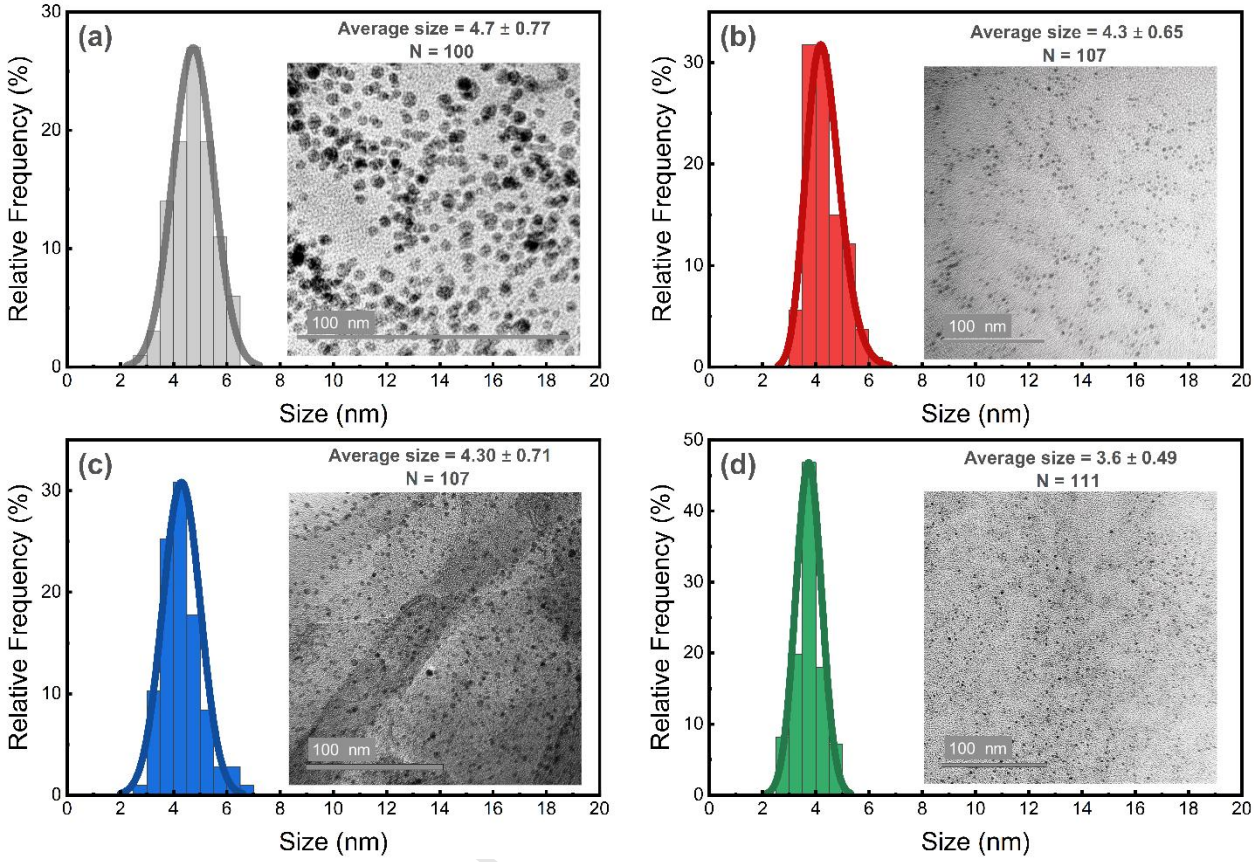


Figure 1. TEM analyses of the GQDs generated via PLAL reveal a narrow size distribution, as illustrated by a histogram with Gaussian profiles (a) for the pure GQDs, (b) for Cl-GQDs system, (c) for N-GQDs system and (d) for S-GQDs system.

Mass yield was evaluated by comparing the dried weight of the final GQD product with the initial mass of carbon precursor employed in the PLAL synthesis. As reported in **Table S1**, N-GQDs exhibited the highest yield of 80.9 %, followed by sulfur variants at 76.9 % and chlorine variants at 70.1 %, compared to 71.6 % for pure GQDs. Because ablation and suspension parameters were identical to those of the previously established protocol [35], these variations in yield are attributed primarily to salt-specific chemistry under cavitation and to diminished thermal stress during drying.

Drying temperature was reduced from 60 °C to 50 °C to minimize evaporation of weakly bound surface species, particularly halogen and sulfur functionalities, thus enhancing material recovery without compromising colloidal stability. Under identical ablation conditions, typical yields at 60 °C drying average approximately 61.5 percent [35]. The optimized 50 °C step increases mean recovery to 74.8 %. This 74.8% value represents the overall mean recovery across all systems at 50 °C. However, individual yields varied depending on precursor chemistry, with N-GQDs reaching 80.9% and Cl-GQDs remaining lower at 70.1% (**Table S1**). The observed improvement is likely due to preservation of carbon, chlorine, and carbon-sulfur bonds that would otherwise cleave or volatilize at higher temperatures while still ensuring efficient solvent removal. The high reproducibility of these yield values and size distributions demonstrates the robustness of the PLAL approach and its potential for scale-up. In particular, increasing laser repetition rates or employing continuous-flow ablation configurations could enable environmentally responsible, high-throughput production of functionalized GQDs while maintaining purity and uniformity.

3.2 Functional Groups and Elemental Composition

The FTIR spectra of the GQDs provide valuable insights into the functional groups present as a result of the synthesis process (**Figure 2**). Notably, the fingerprint region (1000–1500 cm^{-1}) was especially informative for identifying distinct vibrational modes. The spectrum of undoped GQDs exhibited well-defined characteristic bands, including a broad O–H stretching vibration around ~3410 cm^{-1}, a sharp C=O stretching vibration near ~1720 cm^{-1}, and an aromatic C=C stretching mode at ~1625 cm^{-1}. Additional signals were observed at ~1220–1260 cm^{-1} and ~1040–1100 cm^{-1}, corresponding to C–O–C and C–O stretching vibrations, respectively, indicative of oxygen-containing functional groups [35]. Upon heteroatom functionalization (e.g., with Cl, N, or S), significant spectral modifications were observed. These included the

appearance of broader, less-resolved absorption bands and the emergence of new features attributable to heteroatom-related bonding, reflecting structural and chemical alterations in the GQD surface chemistry.

For N-GQDs, several distinct bands emerged. Peaks at approximately 1376 cm^{-1}, 1242 cm^{-1}, 1164 cm^{-1}, and 1074 cm^{-1} were observed, corresponding to various C–N vibrations in aliphatic and aromatic environments, as well as potential N–H bending. These features align with previous reports [59,60], and confirm successful incorporation of nitrogen atoms into the GQD lattice. The presence of these peaks reflects substitutional or edge effects and the formation of stable nitrogen-containing functional groups.

S-GQDs exhibited absorption bands in the 1050–1250 cm^{-1} range, notably near 1150 cm^{-1}, which are typically attributed to C–S stretching or S=O symmetric/asymmetric stretching. These signals may correspond to thiophene-like or sulfonyl groups, although overlap with oxygenated bands prevents unambiguous assignment [61,62]. Additional evidence supports this interpretation, indicating successful sulfur functionalization [63,64]. Notably, these bands can overlap with other oxygen- or halogen-containing moieties, complicating direct identification.

In contrast, Cl-GQDs did not present clear or unique absorption features distinguishing them from pure or S-functionalized samples. This limitation is consistent with the low electronegativity-driven reactivity of chlorine toward the graphene framework, often resulting in low doping efficiency or the formation of labile C–Cl bonds. The low IR activity and overlapping region of C–Cl vibrations (usually around 600–800 cm^{-1}) with broader GQDs background features render chlorine incorporation difficult to verify via FTIR alone [65,66].

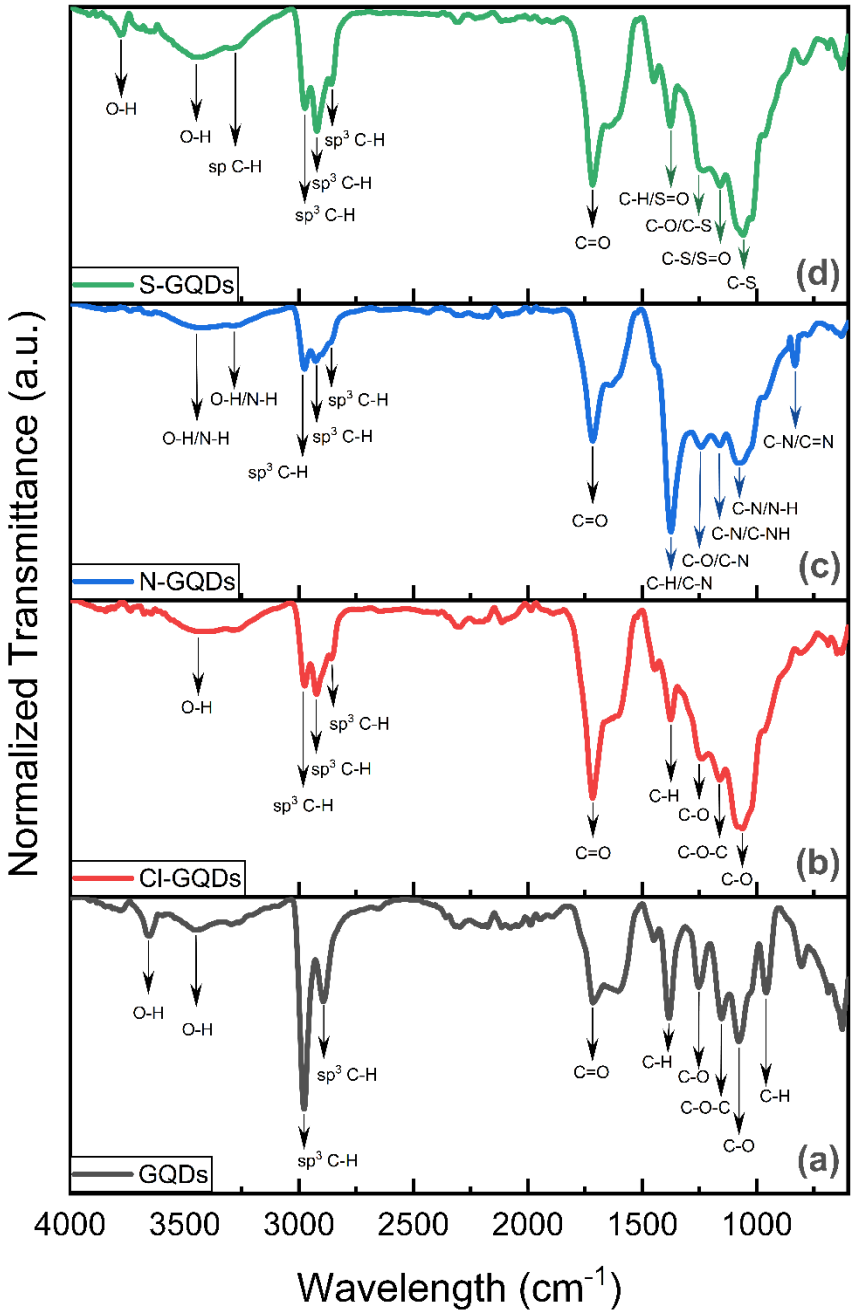


Figure 2. FTIR of samples (a) pure GQDs, (b) Cl-GQDs, (c) N-GQDs and (d) S-GQDs.

While FTIR spectroscopy revealed notable spectral changes upon treatment with chlorine-, nitrogen-, and sulfur-containing precursors, suggestive of surface functionalization by heteroatoms introduced during synthesis, these findings alone are not sufficient to confirm

effective doping. Given that FTIR detects vibrational modes associated with functional groups regardless of their bonding strength or depth of incorporation, the observed features may also arise from surface adsorption or weakly bound molecular residues rather than true substitutional doping within the GQD lattice. Furthermore, the overlapping nature of certain vibrational bands, particularly in the fingerprint region, may lead to ambiguous assignments when multiple functional groups are present. To resolve these uncertainties and verify whether the heteroatoms were covalently integrated into the carbon framework or merely associated with the surface, XPS was employed. Owing to its superior elemental sensitivity and capacity to distinguish between bonding environments, XPS offers a more definitive assessment of dopant incorporation at the atomic level. While FTIR indicated spectral changes consistent with possible N- and S-functionalization, these may also arise from weakly adsorbed or surface-bound species. Therefore, XPS analysis was necessary to distinguish true lattice incorporation from mere surface adsorption.

To assess whether these heteroatoms were covalently incorporated or merely adsorbed, XPS was conducted to investigate the elemental composition and chemical states of the GQDs synthesized via PLAL. The survey spectra (**Figure 3a–d**) revealed clear differences in dopant presence and incorporation efficiency depending on the precursor used during synthesis.

Among the analyzed systems, only the Cl-GQDs sample (**Figure 3b**) exhibited distinct Cl 2p peaks between 198 and 200 eV, corresponding to covalent C–Cl bonding and residual ionic Cl^- species, thus confirming partial substitutional incorporation of chlorine into the GQD lattice [67]. In contrast, the N-GQDs sample (**Figure 3c**) showed a weak and broad N 1s signal near 408 eV, while the S-GQDs sample (**Figure 3d**) displayed no detectable features in the S 2p region. These findings indicate that nitrogen and sulfur were not covalently integrated into the carbon

framework but are instead adsorbed or bound to surface defects and edge sites, reflecting surface functionalization rather than true lattice doping under the applied synthesis conditions.

High-resolution XPS scans further elucidated the bonding nature of the potential dopants (**Figures S1a–c**). For Cl-GQDs, two distinct peaks at 198.4 eV and 200.0 eV were assigned to covalent C–Cl bonding and residual ionic Cl^-, respectively. These results confirm the effective incorporation of chlorine into the GQD structure. In contrast, the N-GQDs spectrum exhibited only a broad signal around 407 eV, attributed to physisorbed oxidized nitrogen species rather than covalent bonding. Nevertheless, as discussed later in the optical analyses, nitrate-derived residues may still influence surface passivation and defect restructuring, indirectly enhancing photophysical properties despite the lack of direct lattice incorporation. Similarly, S-GQDs showed no significant peaks in the S 2p region, confirming the absence of sulfur-carbon interactions[57,67]. The absence of sulfur incorporation does not contradict the FTIR signatures, since sulfite ions influenced the local reaction environment during PLAL. Acting as reductants, they altered oxidation pathways without becoming covalently integrated into the GQD lattice.

The limited incorporation of nitrogen and sulfur is likely due to the low dopant concentration (1 mmol L^{-1}). Previous studies typically employ salt solutions of 1–3 mol L^{-1} to promote more extensive doping [57,68]. In this work, lower precursor levels were deliberately selected to evaluate whether trace dopant concentrations could modulate GQD properties while minimizing ionic contamination that complicates purification. This controlled use of 1 mmol L^{-1} dopant precursors ensures a reproducible and mild reaction environment within the ablation plasma, consistent with sustainable synthesis strategies reported for PLAL systems [37,57]. Employing low dopant levels limits excessive ionic residues, preserves optical and electronic homogeneity, and supports the green, surfactant-free nature of the PLAL process while still enabling measurable surface functionalization effects. Despite the reduced precursor

concentration, successful Cl-doping suggests a favorable interaction between Cl^- ions and the plasma plume during ablation. These findings underscore the critical role of precursor chemistry in dopant incorporation efficiency and highlight chloride as a promising dopant candidate for effective incorporation under mild, environmentally benign conditions.

Journal Pre-proof

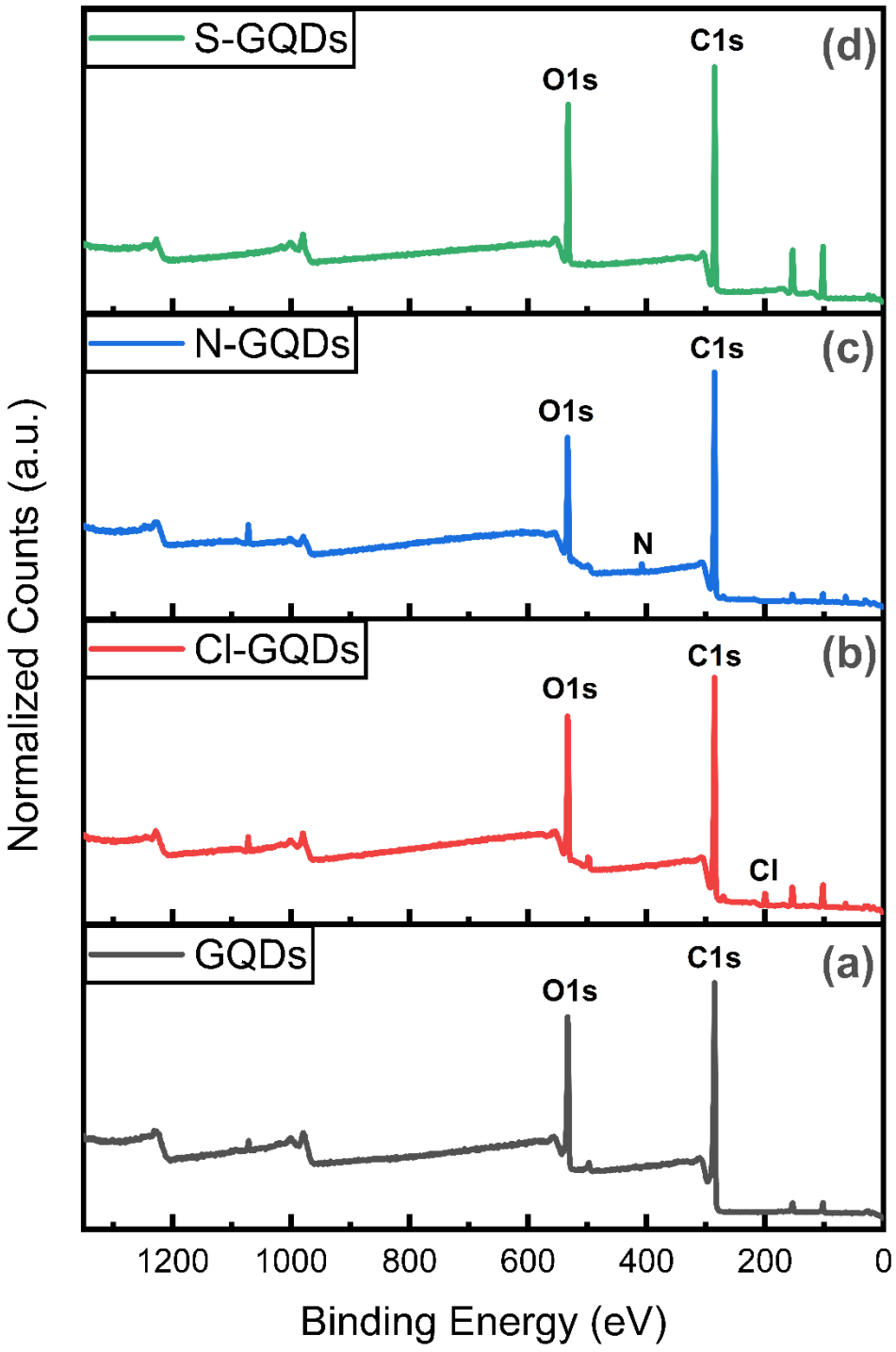


Figure 3. GQD characterizations (a) survey XPS spectra for the GQDs system, (b) survey XPS spectra for the Cl-GQDs system, (c) survey XPS spectra for the N-GQDs system, and (d) survey XPS spectra for the S-GQDs system.

High-resolution XPS analysis of the C1s region (**Figure 4**) was performed to quantify the carbon bonding environments, with the results summarized in **Table 1**. The undoped GQDs exhibited a balanced composition, consisting of 49.16% sp^2-hybridized carbon and 26.27% sp^3-hybridized carbon, along with notable contributions from C–O (17.23%) and moderate contributions from C=O (5.42%) and O–C=O (1.92%) chemical groups. These oxygenated chemical groups are characteristic of laser-ablated GQDs and contribute to their enhanced hydrophilicity and colloidal stability [35,69].

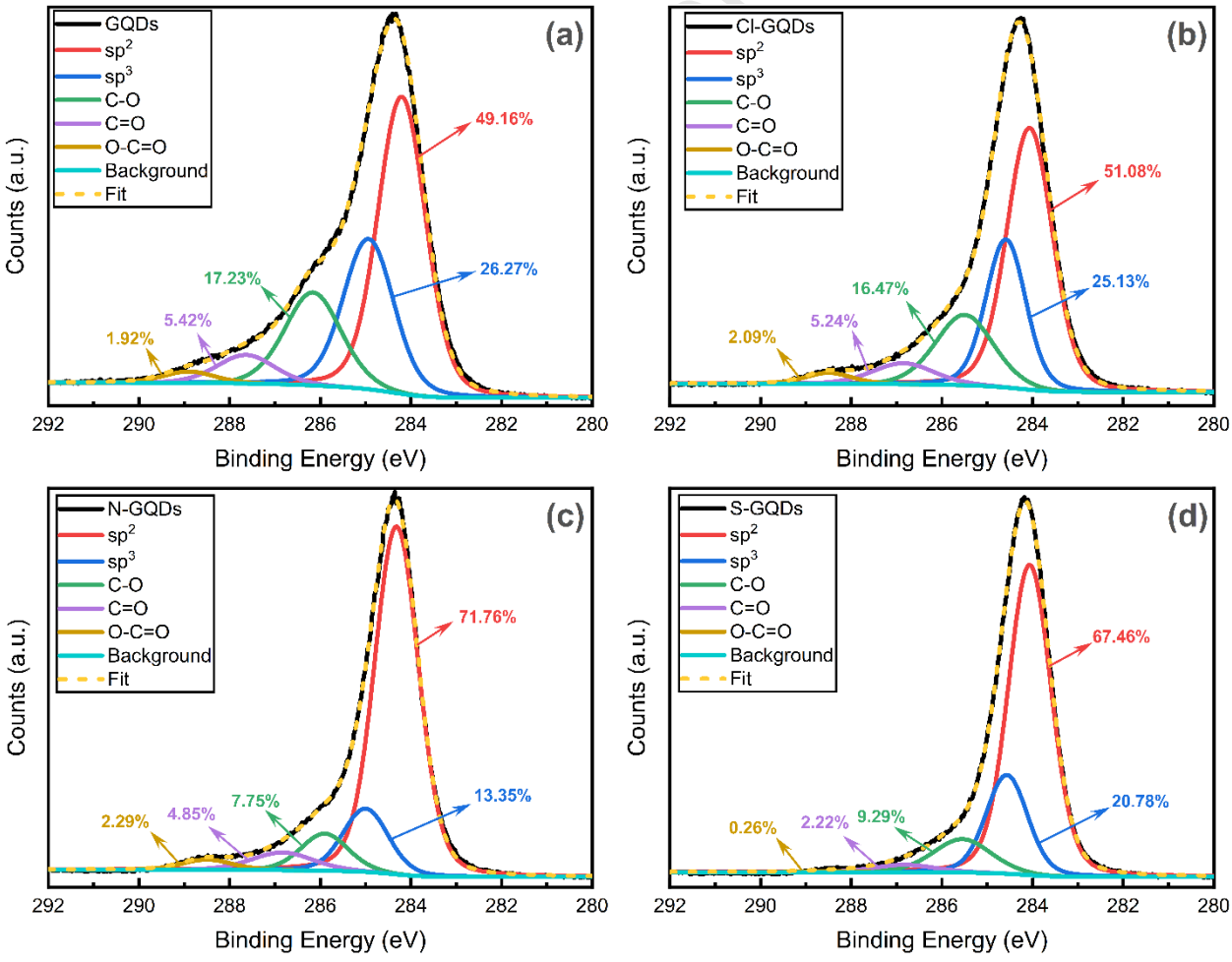


Figure 4. XPS deconvolution of high-resolution C1s binding energy region for (a) GQDs, (b) Cl-GQDs, (c) N-GQDs and (d) S-GQDs.

Cl-GQDs exhibited a modest increase in sp^2-hybridizedcarbon (51.08%) along with a slight reduction in oxygen-containing functional groups. The observed decrease in C–O and C=O groups suggests that chloride ions may have promoted graphitization or acted as radical scavengers, thus preserving conjugated domains through the suppression of overoxidation[70]. The slight increase in O–C=O (2.09%) groups could be attributed to the edge oxidation process or the formation of chlorinated carbonyl species.

The N-GQDs sample displayed a pronounced increase in sp^2-hybridized carbon content (71.76%), accompanied by a decrease in sp^3-hybridized carbon and C–O functional groups. Although direct evidence of nitrogen incorporation was not observed, the enhanced graphitic character indicates that nitrate ions may have promoted selective oxidative etching and structural reorganization. This behavior is likely driven by the reactive nitrogen-derived species, such as NO and NO_2, generated during laser ablation, which can effectively remove disordered carbon regions without directly incorporating nitrogen into the carbon lattice [57,71].

Table 1. Relative percentage of carbon environments derived from C1s deconvolution.

Sample	sp^2 (%)	sp^3 (%)	C–O (%)	C=O (%)	O–C=O (%)
GQDs	49.16	26.27	17.23	5.42	1.92
Cl-GQDs	51.08	25.13	16.47	5.24	2.09
N-GQDs	71.76	13.35	7.75	4.85	2.29
S-GQDs	67.46	20.78	9.29	2.22	0.26

S-GQDs showed an elevated sp^2 carbon content (67.46%) while maintaining a relatively high proportion of sp^3-hybridized carbon (20.78%). The significant reduction in carbonyl functionalities, particularly O–C=O groups (0.26%), suggests that sulfite ions created a reductive environment that effectively suppressed overoxidation. However, this environment did not significantly promote graphitic restructuring. These findings indicate that while SO_3^{2-} ions

mitigate oxidative degradation, they do not facilitate efficient reorganization of the carbon lattice[68,72].

Collectively, the C1s analysis reveals that different anions influence the degree of graphitization and oxidation during PLAL, even at low concentrations. Chloride ions promote moderate graphitization and enable covalent doping. Nitrate ions enhance carbon network reorganization but do not result in nitrogen incorporation, acting mainly through surface functionalization. Sulfite ions function primarily as reductants, suppressing oxidation without providing significant structural refinement. This anion-dependent tunability highlights the potential of salt-assisted PLAL as a versatile approach for tailoring GQD properties through controlled precursor selection.

In summary, the elemental and chemical analyses of GQDs synthesized by PLAL demonstrate that the chemical environment created by different sodium salts plays a pivotal role in controlling graphitization, oxidation, and the balance between doping and functionalization. Chloride ions not only enabled covalent incorporation but also modulated oxidation toward carbonyl group formation. Nitrate ions promoted structural reorganization through surface modification and defect passivation rather than direct lattice incorporation. Sulfite ions influenced the plasma chemistry by creating a reductive environment that limited oxygen incorporation and overoxidation, even though sulfur was not covalently integrated into the GQD lattice. These findings highlight the versatility of salt-assisted PLAL as a strategy for tuning GQD surface chemistry and provide a strong foundation for future studies aimed at optimizing synthesis conditions for targeted functionalization with minimal contamination.

3.3 Optical Properties

The UV–Vis spectra (**Figure S2**) of the analyzed GQDs systems. GQDs typically exhibit strong absorption bands in the deep ultraviolet (UV) region (<250 nm), attributed to π–π*

Journal Pre-proof

electronic transitions within the sp^2-hybridized carbon lattice. In contrast, absorptions at longer wavelengths (>250 nm) are generally assigned to n–π* transitions arising from oxygen-containing surface functional groups [71,73]. All samples display intense absorption at 200–210 nm, indicative of π–π* transitions in the carbon core. The complete absence of absorption above 450 nm confirms that electronic transitions are confined to the UV and blue spectral ranges, suggesting minimal interaction between the forming GQDs and the 1064 nm laser photons used during PLAL process.

The spectra of GQDs, Cl-GQDs, and S-GQDs reveal distinct shoulders at ~230 nm and ~265 nm, corresponding to π–π* transitions in sp^2 domains and n–π* transitions from oxygenated functional groups, respectively. Notably, N-GQDs exhibit an enhanced absorption peak at 210 nm, which may result from nitrate-induced surface modification rather than direct doping [73]. These modifications may enhance transition probabilities and introduce intermediate energy levels, thereby strengthening UV absorption. Furthermore, all GQD variants show weak and featureless absorption between 350 and 450 nm, implying a heterogeneous distribution of surface functional groups.

Edge and size effects often provide the theoretical basis for GQD emission characteristics. Comprehensive two-dimensional photoluminescence analyses produced an excitation–emission matrix covering $\lambda_{exc} = 200–500$ nm and $\lambda_{emi} = 220–700$ nm at the same concentration used in UV–Vis measurements. **Figure S3a-d** shows that the PL analysis of all GQDs, whether pure or functionalized with chlorine, nitrogen, or sulfur, exhibits a pronounced ultraviolet absorption band near 235 nm[74]. This feature originates from π–π* transitions within the sp^2-conjugated domains formed during pulsed laser ablation in ethanol, strengthening the results previously presented from UV-Vis absorption measurements. Secondary absorption peaks appear at approximately 273 nm and 365 nm, where a shoulder around 340 nm is also present

[35,73,75]. These bands reflect n–π* transitions of oxygenated groups such as carbonyl, carboxyl, and hydroxyl, which arise from ethanol decomposition and subsequent surface oxidation. Function atoms that bond at edge sites, such as thiol or sulfate groups for sulfur-GQDs, amine or pyridinic functionalities for nitrogen counterparts, and C–Cl for chlorine ones, may introduce new non-bonding electron pairs in the systems[27,28]. These can feed into the same n–π* manifold, increasing the overall emission intensity in this region without shifting the peak centers. Thus, samples containing heteroatoms often show enhanced shoulder or band amplitudes, even when peak positions coincide.

During pulsed laser ablation in liquid, dopant/functionalization incorporation follows three principal routes: edge decoration, substitutional insertion, or adsorption process [68,76]. A high-temperature plasma plume forms when nanosecond laser pulses strike the carbon black suspension immersed in ethanol containing dissolved precursors (NaCl, $NaNO_3$, or Na_2SO_3). This plasma contains carbon radicals, ethanol fragments, and dopant-derived ions or radicals (Cl·, NO_x·, SO_x·). As the plume cools and cavitation bubbles collapse, carbon atoms recondense into graphitic domains while dopant species bond to undercoordinated edge sites or become trapped within lattice vacancies [57,68,71]. Nitrogen and sulfur, having atomic radii comparable to carbon, can also substitute directly into the hexagonal lattice [76–78]. Exposure to dissolved oxygen during bubble collapse fixes these heteroatoms in place by oxidizing surface sites [57,78].

Specifically, nitrate ions (NO_3^-) decompose within the high-temperature plasma into reactive nitrogen oxides (NO·and NO_2·) that transiently oxidize and etch disordered carbon regions, creating edge vacancies and enabling nitrogen attachment at defect sites [57,79]. These radicals primarily generate amine, pyridinic, or pyrrolic surface groups rather than substitutional N atoms, consistent with the weak N1s XPS signal and enhanced graphitic ordering observed. In

contrast, sulfite ions (SO_3^{2-}) act as mild reductants under plasma conditions, forming transient sulfur oxide radicals (SO_2^- and SO·) that couple with unsaturated carbon radicals during plasma quenching [68]. This leads to the formation of surface C–S and S=O functionalities, producing thiophene-like or sulfonyl groups that introduce localized emissive trap states. Chloride ions (Cl^-), meanwhile, readily form C–Cl bonds through radical recombination with carbon fragments in the plasma, a process confirmed by the Cl 2p XPS doublet (198–200 eV). These plasma-mediated radical reactions collectively govern dopant incorporation during PLAL, where surface-driven edge functionalization predominates over lattice substitution [80].

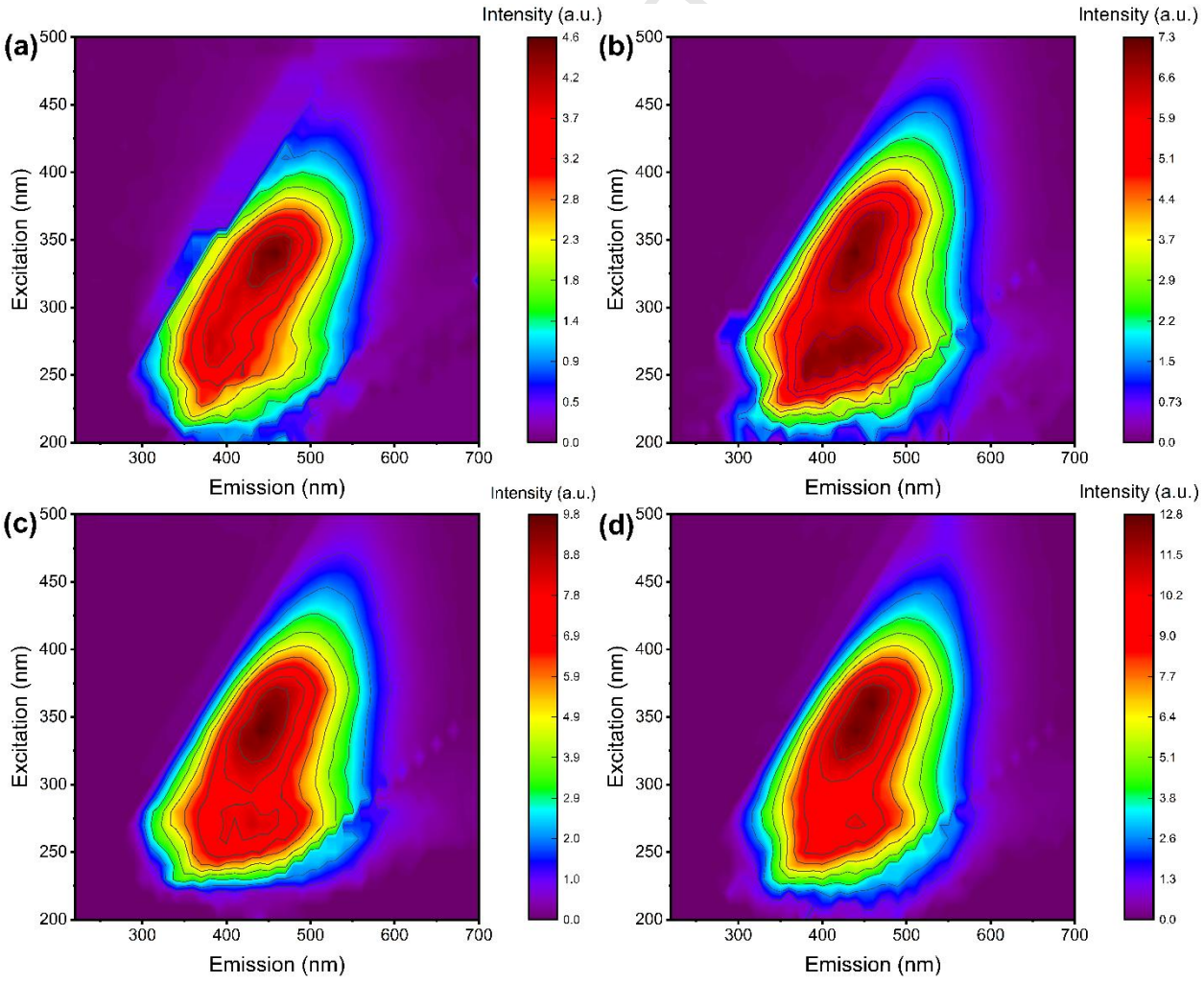


Figure 5. 2D photoluminescence excitation and emission spectra of GQDs in ethanol at 100 μg mL^{-1} (a) pure GQDs, (b) Cl-GQDs, (c) N-GQDs, and (d) S-GQDs.

Figure 5a-d shows two-dimensional fluorescence spectra of graphene quantum dots (GQDs) at 100 μg mL^{-1}. Pure GQDs (**Figure 5a**) exhibit excitation and emission maxima at 340 nm and 460 nm, respectively. Cl-GQDs (**Figure 5b**) display the same primary maxima at 340 nm excitation and 460 nm emission. A secondary excitation band of higher energy, from 250 nm to 270 nm, generates emission between 360 nm and 460 nm. N-GQDs (**Figure 5c**) reproduce the pure profile with maxima at 340 nm and 460 nm. S-GQDs (**Figure 5d**) exhibit two excitation peaks in a single region, the first at 340 nm excitation with 440 nm emission and the second at 360 nm excitation with 460 nm emission.

Heteroatom functionalization of GQDs may introduces new surface electronic and trap states that markedly alter their photoluminescence behavior [81]. GQDs synthesized by laser ablation in liquid exhibit a single strong π–π* transition in the undoped material, with excitation and emission maxima at 340 nm and 460 nm, respectively [30]. Nitrogen adsorption largely preserves this intrinsic profile; nitrate adsorbs into the carbon lattice or decorates edge sites in ways that generate mid-gap states close to the original band, so the 340 nm→460 nm band remains dominant, and no additional features emerge [82]. Chlorine and sulfur, by contrast, give rise to distinct secondary emissive pathways. In Cl-doped GQDs, Cl-related surface sites absorb in the deep-UV (250–270 nm) and relax radiatively over a broad 360–460 nm range, producing a secondary excitation–emission band alongside the native 340 nm→460 nm transition [83]. Sulfur adsorption GQDs display even richer behavior: two separate excitation/emission pairs (340 nm→440 nm and 360 nm→460 nm) could reflect the coexistence of multiple S-site

environments (for example, thiophene-like *versus* oxidized sulfur moieties) that serve as independent radiative centers [68,72].

When these doped and undoped GQDs are dried and then resuspended, they tend to form small aggregates whose photophysics are governed by the competition between aggregation-induced quenching (AIQ) and aggregation-induced emission (AIE) [35,73]. In planar, undoped and N-GQDs, close π–π stacking in clusters opens non-radiative decay channels—exciton hopping and annihilation—so both experience net quenching of their 340 nm→460 nm emission upon aggregation [83,84]. By contrast, Cl- and S- GQDs carry bulky or flexible substituents that prevent perfect π–π overlap and instead restrict intramolecular motions when clustered. This restriction suppresses non-radiative vibrational relaxation and so enhances radiative decay from the Cl- and S-related trap states in wider bands. Consequently, the secondary Cl-derived band in Cl-doped GQDs and the dual S-derived bands in S-functionalized GQDs not only persist but often become more pronounced after drying and resuspension, an archetypal AIE effect that opposes any AIQ of the native π–π* transition [84,85].

Overall, sulfur functionalization modulates the surface electronic structure of GQDs rather than altering their lattice. The introduction of C–S and S=O surface groups generates localized emissive trap states that give rise to dual excitation–emission features (λ_{exc} = 340 nm → λ_{emi} = 440 nm and λ_{exc} = 360 nm → λ_{emi} = 460 nm). These surface states enhance radiative recombination, yielding a higher quantum yield (8.6 %) compared to undoped GQDs (4.2 %), despite the absence of covalent sulfur incorporation. This behavior agrees with previous observations that surface-bound heteroatoms can introduce mid-gap energy levels and improve photoluminescence efficiency in functionalized carbon nanostructures [86].

3.4 Photoluminescence Efficiency and Dynamics

Journal Pre-proof

The QY of GQDs was determined using Rhodamine B as a reference standard (**Table S1**). The pure GQDs synthesized in this study showed an average QY of 4.2%, which aligns with the typical range reported for this type of synthesis [35,87]. In contrast, the doped/functionalized variants demonstrated significantly higher QY values: Cl-GQDs reached 7.3%, N-GQDs 6.2%, and S-GQDs 8.6%. Literature reports indicate that undoped GQDs generally exhibit QY values between 1% and 10%, influenced by variables such as precursor materials, synthesis techniques, and subsequent modifications [35,87]. Incorporating heteroatoms into the GQD structure can introduce additional emissive centers, often resulting in higher QY values compared to pure GQDs, exceeding 10% [74,88,89]. Thus, PLAL synthesis combined with appropriate doping strategies offers a viable route for producing GQDs with enhanced optical properties, making them promising candidates for bioimaging and optoelectronic applications.

The fluorescence-decay kinetics of all four types of graphene quantum-dot (GQD) samples, pure, Cl-doped, N-functionalized, and S-functionalized, were found to be best described by a three-exponential model, as shown in Equation (1). In this model, the ultrafast component τ_1 (0.4–0.5 ns) corresponds to radiative recombination from intrinsic or shallow surface-related trap states, while the longer-lived decay components τ_2 (2.2–2.5 ns) and τ_3 (7.4–8.1 ns) are attributed to exciton recombination influenced by surface functional groups and deeper emissive traps [57]. The model yielded satisfactory goodness-of-fit values ($\chi^2 \approx 1.14$–1.25), supporting its ability to describe the main deactivation pathways in all samples. **Table 2** presents the fluorescence lifetimes and relative amplitudes of the GQDs at 360 nm emission via TCSPC. **Table S3** provides the detailed exponential fitting parameters, and **Figures S4–S7** illustrate the time-resolved fluorescence decay curves.

Journal Pre-proof

Table 2: Fluorescence lifetimes and fluorescence fractions contributions of GQDs and functionalized GQDs at 360 nm of emission, determined by time-correlated single-photon counting (TCSPC).

System	τ_1 (ns)	f_1 (%)	τ_2 (ns)	f_2 (%)	τ_3 (ns)	f_3 (%)
GQDs	0.471	36.3	2.441	44.6	7.759	19.0
Cl-GQDs	0.471	37.2	2.454	44.4	7.842	18.4
N-GQDs	0.524	37.7	2.547	44.9	8.123	17.4
S-GQDs	0.407	36.9	2.257	43.7	7.444	19.3

Pristine, pure GQDs exhibit a dominant intermediate component ($\tau2 \approx 2.44$ ns, $f2 \approx 44.6$ %), followed by the ultrafast component ($\tau1 = 0.471$ ns, $f1 \approx 36.3$ %). The slower $\tau3$ component (7.76 ns, $f3 \approx 19.0$ %) contributes more modestly, resulting in an average lifetime $\langle\tau\rangle \approx 2.74$ ns. This distribution reflects a high density of diverse surface states formed under the employed laser-ablation synthesis conditions [90].

Chlorine doping leads to subtle modifications in the decay dynamics. The $\tau2$ component remains dominant ($f2 \approx 44.4$ %), while $\tau1$ increases slightly to $f1 \approx 37.2$ %. The average lifetime decreases modestly to $\langle\tau\rangle \approx 2.71$ ns. This suggests that Cl atoms act as partial passivating agents, quenching slower emissive states while redistributing excitons toward faster recombination channels [91,92].

In contrast, nitrogen functionalization enhances the radiative contribution of longer-lived states. $\tau2$ remains the major contributor ($f2 \approx 44.9$ %), while $\tau1$ extends to 0.524 ns with $f1 \approx 37.7$ %. $\tau3$ contributes more modestly ($f3 \approx 17.4$ %), producing the longest average lifetime among all samples ($\langle\tau\rangle \approx 2.76$ ns). These results indicate that nitrogen incorporation, particularly in pyridinic or pyrrolic configurations, effectively passivates non-radiative traps and prolongs excitonic recombination [92–94].

Journal Pre-proof

By contrast, sulfur functionalization results in the shortest average lifetime ($\langle\tau\rangle \approx 2.58$ ns). While $\tau 2$ remains the dominant component ($f2 \approx 43.7$ %), $\tau 1$ ($f1 \approx 36.9$ %) and $\tau 3$ ($f3 \approx 19.3$ %) are also significant. This redistribution suggests that sulfur introduces efficient quenching channels, which suppress deeper emissive states even though a fraction persists [68,95,96].

As detailed in Section 2 (Fluorescent Lifetime Decay), the fluorescence decay profiles were analyzed using the multi-exponential model (Equation 1), and the fractional intensity of each emissive population was calculated according to Equation 2. For the S-GQDs sample, the predominance of the intermediate τ_2 component indicates radiative recombination from sulfur-related surface trap states, while the longer-lived τ_3 component represents deeper emissive centers contributing to persistent luminescence. The slight reduction in average lifetime compared with pristine GQDs ($\langle\tau\rangle = 2.74$ ns) reflects partial non-radiative quenching introduced by sulfur functionalities. This trend is consistent with the mechanism proposed by Xu et al. [97], in which sulfur incorporation modulates the balance between radiative and non-radiative decay pathways, enhancing the density of emissive centers while maintaining photostability.

Taken together, these results demonstrate that heteroatom doping and functionalization can be used to tailor the photophysical response of in-liquid laser-synthesized GQDs. Nitrogen incorporation most effectively prolongs excited-state lifetimes by passivating trap states and enhancing radiative decay, making N-GQDs attractive for time-gated imaging and fluorescence sensing. Chlorine has only a modest effect, whereas sulfur dramatically accelerates non-radiative decay, suggesting its use in applications requiring ultrafast quenching or photothermal conversion. Such tunability of τi and fi via surface chemistry offers a versatile route to optimize GQDs for targeted optoelectronic and biomedical technologies.

3.5 Electrochemical Performance and Application Assessment

Journal Pre-proof

GQDs possess outstanding electrochemical properties, including high surface area, excellent conductivity, and abundant edge-plane defects, making them highly suitable for electrochemical sensors. It is important to note that the present work focuses exclusively on the liquid-phase electrochemical sensing of EP and does not include gas-phase adsorption experiments or density functional theory (DFT) modeling. Theoretical concepts are discussed only to provide contextual support for the experimental adsorption and charge-transfer mechanisms. Heteroatom doping or functionalization of GQDs with elements such as chlorine, nitrogen, and sulfur can significantly enhance their electrochemical performance by modulating electronic structure, increasing conductivity, and introducing active surface sites. In this study, GQDs synthesized via PLAL were employed for the detection of EP, benefiting from the high purity and tunable surface chemistry inherent to this method. The colloidal GQDs were deposited onto a glassy carbon electrode (GCE) by drop casting, followed by a small amount of Nafion® to ensure film adhesion, prevent nanomaterial leaching, and promote uniform coverage. Additionally, the sulfonate groups (─SO_3^-) in the Nafion® matrix electrostatically attracted protonated EP molecules to the electrode interface, enhancing signal intensity [11,98]. This configuration effectively combines the electrocatalytic activity of GQDs, the ion-exchange capability of Nafion®, and the performance benefits of heteroatom or functionalization to achieve sensitive and selective electrochemical detection of EP.

To evaluate the electrochemical behavior of the modified electrodes, cyclic voltammetry (CV) and electrochemical impedance spectroscopy (EIS) were performed using EP and hexaammineruthenium solutions, respectively (Figure 6a–b). For electrochemical measurements, epinephrine (EP) solutions were freshly prepared at 1 mmol L^{-1} and diluted to 50 µmol L^{-1} for voltammetric testing, a concentration that provides well-defined oxidation and reduction peaks within the linear response range of the modified electrodes. CV experiments

were carried out at a scan rate of 50 mV s^{-1} in 0.1 mol L^{-1} Britton-Robinson buffer solution (pH 4.0). The unmodified GCE exhibited an anodic peak at +0.66 V with a corresponding current of 1.07 ± 0.01 μA. When the GCE was modified with Nafion®, the voltammogram displayed an anodic peak at +0.50 V (Ip = 2.00 ± 0.31 μA) and a cathodic peak at +0.17 V (Ip = −1.91 ± 0.06 μA). This behavior is attributed to the ion-exchange characteristics of Nafion®, which favor electrostatic attraction between its sulfonate ($–SO_3^-$) groups and protonated epinephrine species, enhancing redox activity [98]. lectrodes modified with GQDs synthesized via PLAL demonstrated further improvements in electrochemical response. Among these, the electrodes incorporating GQDs produced in the presence of 1 mmol L^{-1} Na_2SO_3 exhibited the highest anodic and cathodic peak currents (4.70 ± 0.16 μA and −4.46 ± 0.20 μA, respectively), indicating that GQD incorporation significantly enhances electron transfer kinetics and overall sensing performance.

The improved electrochemical behavior of the GQDs/Nafion® composites arises from the complementary roles of both components. Nafion®, a perfluorinated cation-exchange polymer, preconcentrates positively charged epinephrine molecules via electrostatic attraction between its sulfonate ($–SO_3^-$) groups and the analyte, thereby enriching the local concentration of EP near the electrode surface. The embedded GQDs contribute by providing high electrical conductivity and abundant π–π interaction sites with the aromatic ring of epinephrine, facilitating charge transfer and enhancing signal intensity. This cooperative effect between Nafion® and GQDs accelerates electron exchange across the electrode–solution interface, improving redox kinetics and analytical sensitivity, consistent with prior studies on Nafion®–nanocarbon composites [98].

Additionally, the homogeneous dispersion of S-GQDs within the Nafion® matrix, supported by their colloidal stability and nanoscale uniformity, ensures continuous electron-

transport pathways and reproducible signal responses, consistent with previous Nafion–carbon nanocomposite systems [99,100].

The enhanced sensitivity of the Nafion®-GQDs composites for EP detection stems from carefully engineered electrostatic and electrochemical interactions. The S-GQDs system's success arises from its negative surface charge ($\zeta = -16.4$ mV), which balances two critical factors: electrostatic attraction of protonated EP (at pH 4.0) to Nafion®'s sulfonate groups ($-SO_3^-$) and minimized repulsion between S-GQDs and the negatively charged polymer matrix, as presented in **Figure S8** [98]. The slightly oxidized surface of the S-GQDs further improves electron transfer kinetics, likely due to the higher density of electroactive sites. By contrast, GQDs with lower surface charge (e.g., N-GQDs, $\zeta = -4.1$ mV) introduce destabilizing repulsion, whereas moderately charged variants (e.g., Cl-GQDs, $\zeta = -13.0$ mV) offer weaker electrostatic preconcentration. These results highlight the importance of optimizing GQD surface charge to harmonize with Nafion®'s ion-exchange characteristics.

The superior electrochemical response of the S-GQDs arises from their negatively charged, sulfur-functionalized surfaces rather than true lattice doping. XPS analysis (Figure 3 and Figure S1c) confirmed the absence of distinct S 2p features associated with covalent S–C or S=O bonds, indicating that sulfur species are not incorporated into the graphitic lattice but are instead weakly adsorbed on the GQD surface. These surface-bound sulfate and sulfite groups, derived from Na_2SO_3 during the PLAL process, interact through physisorption, hydrogen bonding, and Coulombic attraction with oxygenated moieties (C=O, C–OH) on the GQD edges. Such physisorptive interactions modify the surface energy and polarity of the nanomaterial, enabling strong interfacial compatibility with the sulfonate ($-SO_3^-$) domains of Nafion®. This interfacial coupling promotes uniform film formation and efficient charge mediation at the glassy carbon electrode. Consequently, the binding energy within the GCE/Nafion®/S-GQDs architecture

originates primarily from these weak electrostatic and hydrogen-bonding interactions rather than covalent sulfur–carbon linkages, consistent with reports describing surface-mediated charge tuning in laser-synthesized carbon nanostructures [97].

The selective interaction of the composite material with charged species was further confirmed using hexamine ruthenium, a positively charged redox probe. As illustrated in **Figures 6c** and **6d**, EIS indicated a notable rise in charge-transfer resistance (R_{ct}) for electrodes modified with the Nafion®-GQDs composites compared to the unmodified GCE. This increase in R_{ct} is likely due to the adsorption of cationic molecules onto the negatively charged surfaces of the Nafion®-GQDs matrix. Both GQDs and Nafion® carry negative charges, enabling them to effectively retain cations within the film, thereby limiting their transport to the electrode interface [101]. Nevertheless, the CV results (**Figure 6b**) showed an enhanced peak current, which can be attributed to the large surface area and catalytic activity of GQDs that enhance redox processes once the initial charge barrier is surpassed [100]. Additionally, Nafion®'s ion-exchange capabilities may promote the accumulation of cations near the electrode, increasing the local concentration of the redox species within the composite layer [101]. The observed variations in redox peaks intensity and position during CV are likely a result of heterogeneous electron transfer dynamics introduced by the nanocomposite, as well as diffusion and charge transport constraints within the modified structure [102].

The influence of Nafion® film concentration on electrochemical performance has been extensively investigated in proton-exchange membranes and catalytic layer systems [103–105], and similar considerations apply to its role in electroanalytical electrodes. In this context, the thickness and morphology of the Nafion® film are critical determinants of ionic conductivity and analyte accessibility. Extremely thin coatings tend to exhibit low ionic conductivity and limited preconcentration capacity, whereas excessively thick films hinder both proton and electron

transport, increasing ohmic resistance and slowing electrode kinetics [105]. In the present study, a Nafion® concentration of 0.15% (w/v) was chosen as an optimal compromise. This composition produced a continuous yet relatively thin film that facilitated efficient EP^+ accumulation while maintaining low charge-transfer resistance and good proton mobility. The interferogram of the GCE coated with 0.15% Nafion® (**Figure S9**) revealed an average central thickness of approximately 4 µm, gradually tapering toward the electrode edges. Such morphology, characteristic of solvent-cast Nafion® layers, promotes rapid mass transport and a uniform electrochemical response across the electrode surface.

Journal Pre-proof

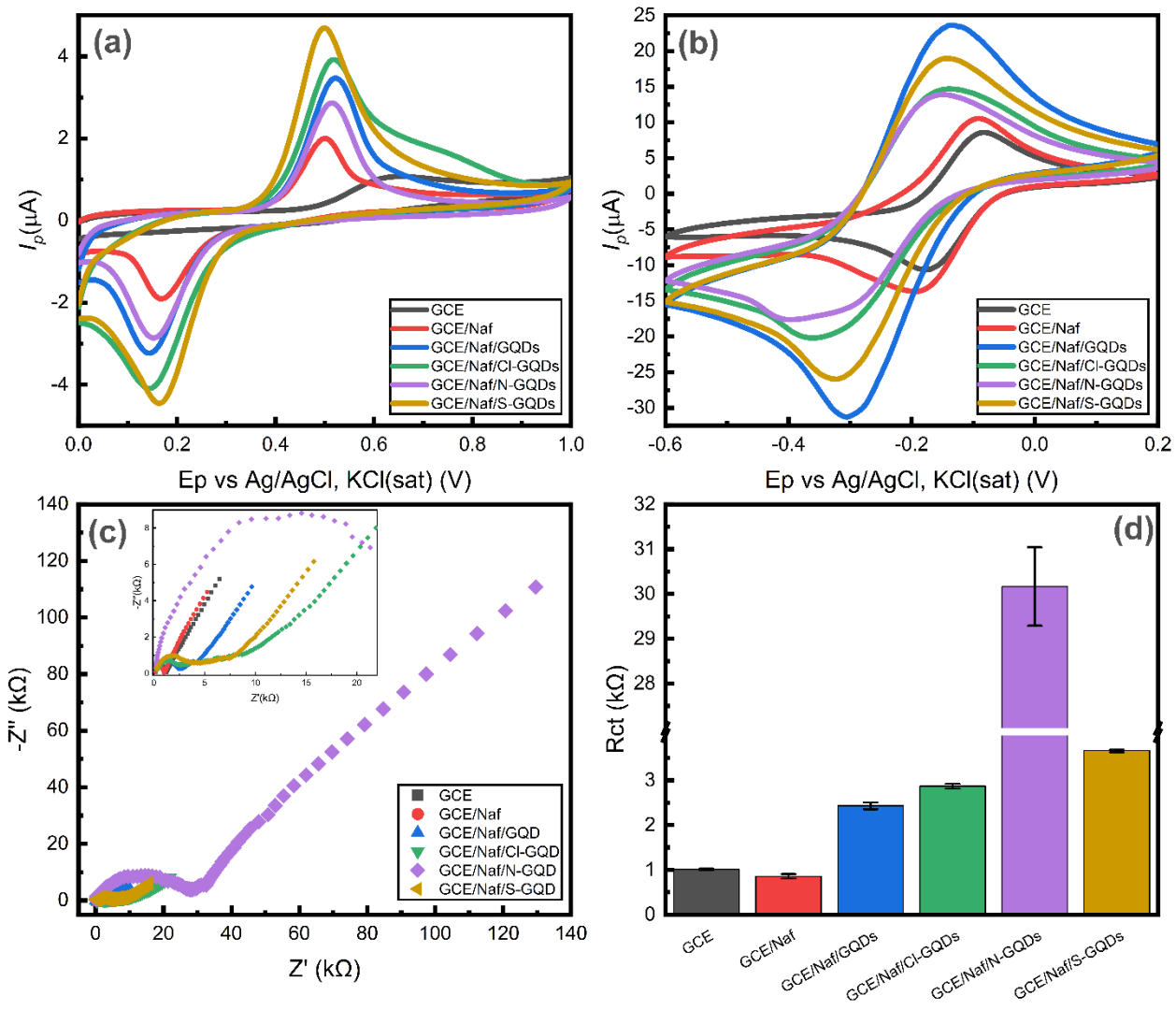


Figure 6. Electrochemical application of GQDs as a sensor for EP and electrochemical correspondent characterization (a) Voltammetry analysis for 50 µM of EP for GCE (black curve), GCE/Nafion® (red), GCE/Nafion®/GQDs (blue), GCE/Nafion®/Cl-GQDs (green), GCE/Nafion®/N-GQDs (purple) and GCE/Nafion®/S-GQDs (dark yellow), B-R buffer solution at pH 4.0, (b) CV analysis of hexamineruthenium chloride [Ru $(NH_3)_6$] Cl_3 (III) and hexaammineruthenium chloride [Ru $(NH_3)_6$] Cl_2 (II) in a 0.1 mol L^{-1} KCl solution, (c) EIS using hexamineruthenium (III)/ hexaammineruthenium (II) in a 0.1 mol L^{-1} KCl solution and (d) Calculated R_{ct} for the materials based on Randles-Circuit.

The EIS data, analyzed using a Randles equivalent circuit (**Figure S10**) and summarized in **Table S4**, revealed an increase in Rct at high frequencies and diffusion-limited behavior at low frequencies, consistent with the function of Nafion® as a charge-selective barrier [101]. This behavior facilitates the preferential accumulation of cationic analytes such as EP while restricting interferents, enhancing selectivity in complex matrices. Sulfur functionalization of GQDs was performed via PLAL, a method that yields ultra-pure, surfactant-free nanomaterials. During ablation in sulfur-containing media, sodium sulfate may be adsorbed onto the GQDs, modifying their electronic properties, increasing surface charge, and improving redox activity [106]. These alterations in interfacial chemistry strengthen electrostatic interactions with target species and promote more efficient electron transfer, contributing to enhanced electrochemical sensing performance under biologically relevant conditions.

Moreover, CV demonstrated that both GQDs and S-GQDs-modified electrodes preserved stable anodic and cathodic responses over consecutive measurements (n = 3), confirming excellent interfacial stability within the Nafion® matrix. The π–π stacking between GQDs and the polymer backbone, combined with electrostatic coupling through sulfonate groups, maintains efficient charge-transfer pathways during repeated operation. This robust interface ensures durable electrochemical performance comparable to that reported for other carbon–Nafion® composites [102,107].

This interfacial robustness is further supported by the intrinsic chemical purity of the nanomaterials. The GQDs and S-GQDs obtained via PLAL are free of residual acids, surfactants, or metallic impurities, as verified by XPS and FTIR analyses, ensuring biocompatibility and minimal environmental risk. The sulfur-functionalized GQDs (S-GQDs) contain only surface-

bound sulfate and sulfonate groups, not lattice-incorporated dopants, which significantly reduces ecotoxicity compared with chemically doped nanocarbons.

The use of surface-sensitive redox probes in the characterization of electrochemical sensors necessitates careful analysis, as interactions between the probe and the electrode surface can significantly affect the observed R_{ct}. Even substrates with high intrinsic conductivity, such as glassy carbon (GC), may display elevated R_{ct} values if electron transfer is impeded by unfavorable interfacial interactions, potentially leading to an underrepresentation of the material's inherent electrochemical performance. The need for analyte-specific evaluation is highlighted by findings such as those reported by Ricardo et al. (2025) [98], where gold nanoparticles (AuNPs) synthesized by PLAL using $NaNO_3$ demonstrated improved detection of serotonin compared to AuNPs synthesized in the presence of other salts. In the present study, results indicate that even PLAL-derived GQDs require case-specific optimization depending on the target analyte, as residual ions from the synthesis medium (e.g., Cl^-, NO_3^-) can compete with analyte adsorption. For example, GQDs synthesized in a sulfur-containing medium showed enhanced EP detection (4.70 µA), attributed to sodium sulfate adsorption effects that can facilitate electron transfer. In contrast, GQDs prepared in nitrogen-based systems exhibited lower sensitivity due to competitive adsorption of sodium nitrate species into the GQD structure, which may obstruct access to catalytically active sites. These observations underscore the importance of considering both nanomaterial purity and the complex interaction between synthesis conditions and analyte adsorption dynamics in sensor development.

GQDs synthesized via PLAL offer key advantages over those produced by chemical methods, particularly in terms of purity, surface reactivity, and doping control. Chemical synthesis typically involves harsh reagents and high-temperature conditions, which can introduce residual contaminants and undesired functional groups [108]. In contrast, PLAL is a single-step,

surfactant-free process conducted under ambient conditions, yielding cleaner nanomaterials with accessible active sites and minimal environmental impact. When performed in dopant or functionalization containing media, PLAL enables the direct incorporation of heteroatoms, such as chlorine, or salts as sodium sulfate, and sodium nitrate, into the GQD structure, resulting in uniform material without the by-products commonly associated with chemical routes [98,109]. This approach allows for better control of surface and electronic properties, enhancing the electrochemical performance of GQDs in sensing applications.

The bonding configurations and surface characteristics of the pristine and heteroatom-functionalized GQDs, derived from FTIR and XPS analyses, directly influence their electrochemical stability. Pure GQDs contain abundant oxygenated groups (C–O, C=O) that promote hydrophilicity but also increase oxidative susceptibility. Cl-GQDs show covalent C–Cl bonds and slightly higher graphitization, improving conductivity. N-GQDs exhibit greater sp^2 hybridization and C–N bonding, enhancing electron mobility but retaining residual oxidation sites. In contrast, S-GQDs combine high sp^2 content with minimal O–C=O species, yielding a more conjugated and stable carbon network. These structural distinctions explain the superior and more stable redox response of S-GQD-modified electrodes in cyclic voltammetry, as sulfur functionalities and extended π–π conjugation facilitate charge transfer and suppress surface oxidation. Overall, dopant-induced modulation of bonding and graphitic order governs both the electronic and electrochemical robustness of the PLAL-synthesized GQDs.

3.6 Influence of pH and Electrolyte Composition

The influence of pH on EP detection was examined using CV across the pH range of 2.0 to 8.0. This interval was chosen to maintain EP predominantly in its protonated form (pKa ≈ 8.6), facilitating electrostatic interactions with the sulfonate groups of Nafion®, while avoiding pH extremes that could compromise the electrochemical sensor's stability [99,110]. Measurements

were conducted in Britton-Robinson buffer solution (0.1 mol L^{-1}). As shown in **Figure S11a-c**, the anodic peak current increased from pH 2.0 to 4.0, accompanied by a decrease in cathodic current intensity. Beyond pH 4.0, the anodic current progressively declined, and cathodic responses diminished significantly, becoming negligible at pH values above 5.0. The anodic peak potential exhibited a negative shift with increasing pH, consistent with a proton-coupled electron transfer mechanism involved in EP oxidation. Among the tested conditions, pH 4.0 produced the highest anodic current (10.39 µA) and a well-defined voltametric peak. This sharper peak contributes to better resolution of EP oxidation from potentially interfering redox processes. The results suggest that pH 4.0 provides a suitable balance between electrostatic preconcentration, electron transfer kinetics, and voltametric peak resolution. Consequently, pH 4.0 was selected for subsequent analytical measurements.

The observed decrease in current from pH 4.0 to 5.0 may be explained by a reduction in proton availability in conjunction with the interaction between the Nafion® polymer and the GQDs. The sulfonate groups of Nafion®, together with the negatively charged surfaces of GQDs, contribute to the retention of cationic species, such as H^+, within the polymeric matrix. This retention limits the diffusion of cations toward the electrode surface, thereby diminishing the redox current detected by cyclic voltammetry. As the pH increases, although electrostatic interactions between the negatively charged components and cationic species persist, the overall decrease in free proton concentration leads to a lower retention of cations within the matrix [98]. This reduction facilitates the diffusion of redox-active species to the electrode interface, contributing to the slight recovery in current observed at pH 5.0.

3.7 Electrochemical Kinetics and Mechanistic Insights

The investigation of the effect of scan rate variation is essential for elucidating key aspects of the electrochemical reaction mechanism and sensor performance, as well as for

identifying optimal conditions for EP determination. The influence of the scan rate on the electrochemical response of EP at the GCE/Nafion®/S-GQDs sensor was investigated using CV. It was observed that the peak currents increased progressively with increasing scan rate, ranging from 25 to 150 mV s^{-1} (**Figure S12a**).

To analyze the charge transfer kinetics, the anodic peak current (I_{pa}) was plotted against both the square root of the scan rate ($v^{1/2}$) and the scan rate (v), yielding two distinct linear correlations with coefficients of determination (R^2) of 0.9942 and 0.9958, respectively. This dual linearity indicates that the electrochemical process is governed by a combination of diffusion and adsorption mechanisms (**Figure S12b**) [11,111]. A similar trend was observed for the cathodic peak current (I_{pc}), which also displayed strong linearity with both $v^{1/2}$ and v, with R^2 values of 0.9945 and 0.9956, further supporting the involvement of mixed mass transport processes (**Figure S12c**).

To corroborate these findings, logarithmic plots of Ipa and Ipc versus scan rate were constructed (**Figure S12d**). The anodic current showed a linear relationship (R^2 = 0.9995), described by the equation log Ipa = 0.844 log v + 1.999. The slope value of 0.844 lies between the theoretical limits for diffusion-controlled (slope ≈ 0.5) and adsorption-controlled (slope ≈ 1.0) processes, indicating a mixed control mechanism, as reported in previous studies [11,98,111]. Similarly, the cathodic current exhibited a linear fit (R^2 = 0.9981), with the equation log Ipc = 0.914 log v + 2.054. The slope value of 0.914 suggests a predominantly adsorption-controlled reduction process. These results imply that the oxidation of EP at the GCE/Nafion®/S-GQDs interface is regulated by both diffusion and adsorption mechanisms, while the reduction process is mainly driven by adsorption.

These experimental findings align well with theoretical predictions regarding the adsorption and charge-transfer behavior of heteroatom-functionalized graphene quantum dots.

Journal Pre-proof

Density functional theory studies have shown that nitrogen and sulfur doping substantially modify the electronic structure of GQDs, introducing localized polar sites and enhancing π-electron delocalization across the sp^2 lattice [112,113]. These modifications increase the surface dipole moment and strengthen electrostatic and van der Waals interactions, with DFT-calculated adsorption energies for doped GQDs typically ranging between −0.25 and −0.45 eV. Such theoretical results corroborate the experimentally observed strong preconcentration of epinephrine at the negatively charged Nafion®/S-GQDs interface and the efficient electron-transfer processes reflected in the enhanced oxidation currents. Consequently, the synergistic influence of sulfur-induced surface polarization and extended conjugation provides a sound explanation for the high redox sensitivity and reproducibility demonstrated by the developed sensor.

The observation of dual linearity between current and both scan rate (ν) and $\nu^{1/2}$ further supports that the electro-oxidation of EP at the Nafion®/S-GQDs interface does not follow a purely diffusion-limited process, as would be expected for freely diffusing species, nor a strictly adsorption-controlled process typical of strong surface confinement. Instead, the system operates under a hybrid regime: EP molecules are partially preconcentrated at the electrode surface through electrostatic interactions with the negatively charged sulfonate groups of Nafion® and the surface functionalities of S-GQDs, while additional EP remains accessible in bulk solution [98]. This dual contribution enhances local analyte concentration at the interface, increasing sensitivity, while bulk diffusion ensures continuous replenishment of EP molecules. Such adsorption/diffusion coupling is advantageous for sensing applications, as it combines the selectivity of adsorption with the linear dynamic range of diffusion-controlled processes. The predominance of adsorption in the cathodic pathway (slope ≈ 0.91) further suggests that once EP

is oxidized, its reduced species may interact more strongly with the Nafion®/GQD matrix, possibly through π–π stacking or hydrogen bonding, leading to surface retention that governs the reduction process [114,115].

Moreover, an increase in both anodic and cathodic peak potentials (E_p) was observed as the scan rate increased, indicating kinetic limitations in the electron transfer process. The electron transfer coefficient (α) was estimated by evaluating the shift in anodic peak potential with respect to the logarithm of the scan rate. A linear relationship between Ep and log(v) was established (**Figure S13**), which allowed for further analysis using Laviron's theory. Based on this approach, Equations (3) and (4) were applied, respectively, to estimate the number of electrons involved in the electrochemical oxidation and reduction of EP:

$$o = \frac{2.303\ RT}{(1-\alpha)nF} \quad (3)$$

$$p = \frac{2.303\ RT}{\alpha nF} \quad (4)$$

Where (*o*) and (*p*) are the slopes, (n) is the number of electrons transferred, (R) is the universal gas constant (8.314 J mol^{-1} K^{-1}), (T) is the temperature (298 K), (F) is the Faraday constant (96,485 C mol^{-1}), and (α) is the electron transfer coefficient. According to established literature, for irreversible electrochemical systems, α is typically approximated as 0.5 [11,98,116]. Using this assumption, the number of electrons exchanged during EP oxidation and reduction at the sensor interface was calculated to be 0.80 and 0.87, respectively, close to 1. These results support a one-electron oxidation mechanism for EP, which leads to the formation of a semi-quinone intermediate, identified as leucoadrenochrome-o-semiquinone. This radical species subsequently undergoes a second electron transfer step, producing adrenochrome, a more stable oxidation product [45]. The findings underscore the suitability of the GCE/Nafion®/S-

GQDs sensor for investigating EP's electrochemical pathways, while also providing meaningful insights into the associated charge transfer and mass transport processes.

In summary, the detection of EP at the GCE/Nafion®/S-GQDs interface is governed by a synergistic adsorption–electron transfer mechanism. At pH 4.0, EP exists mainly as a protonated cation ($pK_a \approx 8.6$), which is electrostatically attracted to the negatively charged sulfonate ($–SO_3^-$) groups of Nafion® and the surface of S-GQDs ($\zeta = –16.4$ mV). Simultaneously, π–π stacking between the aromatic rings of EP and the conjugated carbon domains of S-GQDs enhances molecular preconcentration at the electrode surface. The subsequent redox process follows a two-step, quasi-reversible mechanism, where EP undergoes an initial one-electron oxidation to form the leucoadrenochrome semiquinone intermediate, followed by a second electron transfer leading to adrenochrome formation [45]. The calculated electron number ($n \approx 0.8–0.9$) and linear Laviron correlation confirm this pathway. The Nafion®/S-GQDs composite exhibits high structural stability and reproducible voltammetric behavior due to strong π–π and electrostatic coupling between the polymer matrix and the embedded GQDs, maintaining intimate contact and efficient charge mediation. These results align with previous reports showing that Nafion–carbon hybrid films enable adsorption-controlled electrocatalysis and stable redox cycling through synergistic charge mediation at the polymer–nanocarbon interface [99,107].

3.8 Analytical Performance for Epinephrine Detection

The EP determination was carried out by CV in a potential window between 0.0 and + 1.0 V (*vs.* $Ag/AgCl_{(sat.)}$). Voltammograms were recorded as the EP concentration increased incrementally, and the corresponding current responses were analyzed (**Figure 7a**). The calibration curve shown in **Figure 7b** demonstrates a linear response over the concentration range of 0.1 to 10 μmol L^{-1}. The linear relationship between the EP concentration ([EP]) and the

Journal Pre-proof

peak currents was established as follows: for the anodic peak current (I_{pa}), I_{pa} (μA) = 0.129 × [EP] (μmol L^{-1}) − 0.011 (R^2 = 0.9924), and for the cathodic peak current (I_{pc}), I_{pc} (μA) = −0.128 × [EP] (μmol L^{-1}) + 0.033 (R^2 = 0.9953). It is important to note that each calibration point was measured in triplicate, with the GCE/Nafion®/S-GQDs electrode surface being renewed before every measurement.

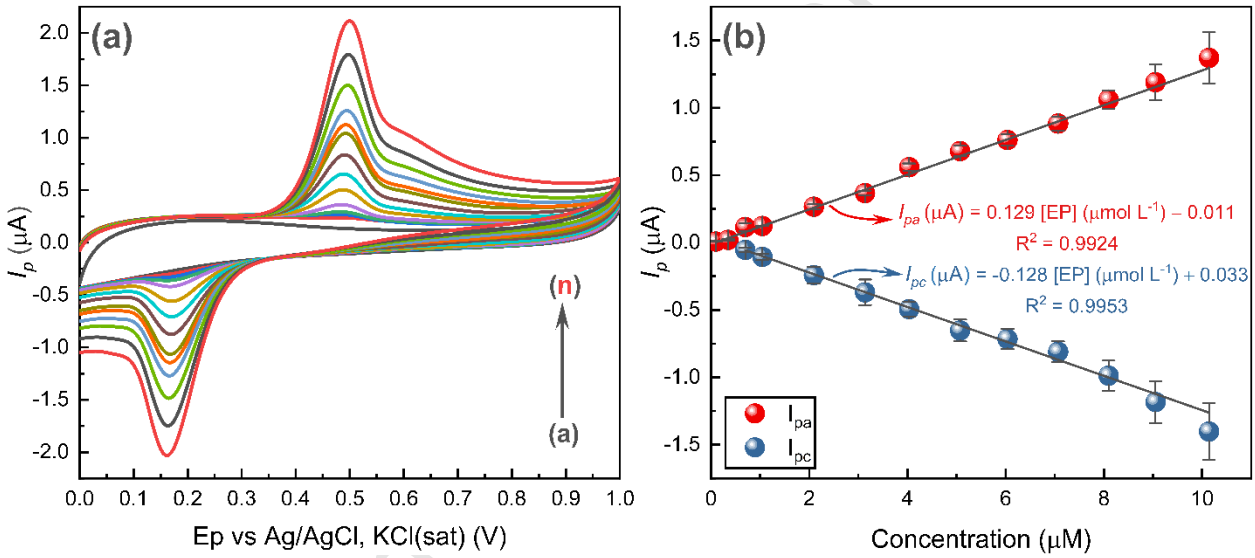


Figure 7. Calibration curve of EP for GCE/Nafion®/S-GQDs sensor. (a) CV measurements at varying EP concentrations (0.1 to 10 μM) and (b) Correlation between the anodic and cathodic peak currents and the concentration of EP.

The theoretical limits of detection (LOD) and quantification (LOQ) were estimated using the standard equations: LOD = 3.3 × Sa / b and LOQ = 10 × Sa / b, where Sa represents the standard deviation of ten blank measurements, and b corresponds to the slope of the linear regression curve [117]. Based on these calculations, the LOD and LOQ values derived from the oxidation calibration curve were 77.6 nmol L^{-1} and 235.1 nmol L^{-1}, respectively. For the

reduction calibration curve, the calculated LOD and LOQ were 78.2 nmol L^{-1} and 237.0 nmol L^{-1}, respectively.

The sharp and well-defined voltammetric peaks, together with the minimal potential separation between oxidation and reduction processes, indicate fast response and recovery dynamics, consistent with sub-second electron-transfer behavior typically observed in GQD-based electrochemical sensors [118].

This enhanced analytical response also reflects the intrinsic sensitivity and selectivity of the S-GQDs surface, where sulfur-induced polarity and π–π interactions promote preferential adsorption of protonated EP molecules under the working conditions. These interfacial effects further contribute to the low detection limits achieved in this study [99].

To contextualize the analytical performance of the developed GCE/Nafion®/S-GQDs sensor, **Table 3** summarizes representative EP electrochemical sensors based on carbon nanomaterials and GQDs.

Journal Pre-proof

Table 3. Comparison of recent electrochemical sensors for epinephrine determination.

Technique	Modifier	Linear range (µmol L^{-1})	LOD (µmol L^{-1})	Real sample	Reference
DPV	$NiO/CuCo_2O_4$/GQDs	0.02 – 2 10 – 500	0.0117	Artificial sweat; urine	[119]
DPV	CQDs/CuO	10 – 100	15.99	EP injection; chicken blood serum	[120]
CA	N–GQD/PEDOT/CuO/Cu mesh	10 – 220	0.088	Urine	[121]
CA	B,N–GQD/PEDOT/CuO/Cu mesh	10 – 220	0.084	Urine	[121]
SWV	GQDs–Chi	0.36 – 380	0.0003	Human blood serum; EP injection	[122]

DPV	AuNC/GQDs/Si	0.01 – 4	0.01	Human urine; DA injection	[123]
CV	Nafion®/S-GQDs	0.1–10	0.077	-	This work

Abbreviations: CA – chronoamperometry; SWV – square wave voltammetry; DPV – differential pulse voltammetry; CV – cyclic voltammetry. *Modifiers:* NiO/$CuCo_2O_4$/GQDs: nickel oxide–copper cobalt oxide–graphene quantum dots nanocomposite conductive ink on a screen-printed electrode; CQDs/CuO: carbon quantum dots decorated copper oxide nanoparticles on a glassy carbon electrode; N–GQD/PEDOT/CuO/Cu mesh: nitrogen-doped graphene quantum dots embedded in poly(3,4-ethylenedioxythiophene) film on a CuO-treated copper mesh; B,N–GQD/PEDOT/CuO/Cu mesh: boron and nitrogen co-doped graphene quantum dots incorporated into a PEDOT matrix on a CuO/Cu mesh; GQDs–Chi: graphene quantum dots dispersed in a chitosan matrix on a carbon paste electrode; AuNC/GQDs/Si: gold nanoclusters anchored to graphene quantum dots functionalized via a silane coupling agent on a glassy carbon electrode; S-GQDs/Nafion®: sulfur-functionalized graphene quantum dots entrapped in a Nafion® film on a glassy carbon electrode.

The proposed PLAL-derived GCE/Nafion®/S-GQDs sensor demonstrates a competitive detection limit (LOD = 77 nM) and a broad linear range (0.1–10 µM), rivaling or surpassing several multi-component hybrid sensors prepared via hydrothermal or chemical oxidation methods. Importantly, the salt-assisted PLAL synthesis is a green, one-step, surfactant-free process that produces GQDs without toxic reagents or post-treatment. The incorporation of Nafion® further enhances epinephrine preconcentration through electrostatic attraction of EP^+ species, boosting sensitivity and selectivity. This synergy enables nanomolar-level detection with a minimal material architecture, positioning the S-GQDs/Nafion® system among the most sustainable and facile electrochemical platforms for epinephrine sensing reported to date.

The results obtained in this study are encouraging, especially when compared with those reported in previous works [124–126]. It is worth noting that while cyclic voltammetry is widely used for preliminary evaluation of electrochemical sensors, it generally offers lower sensitivity compared to techniques like SWV and DPV, as employed in the referenced studies. Therefore, it

is reasonable to suggest that the performance of the sensor could be further enhanced by optimizing the electroanalytical technique used for detection.

Journal Pre-proof

Journal Pre-proof

4. CONCLUSIONS

We demonstrated a sustainable strategy to engineer GQDs through salt-assisted PLAL. The approach successfully incorporated chloride into the carbon lattice, while nitrogen and sulfur treatments primarily induced surface functionalization rather than lattice doping. These modifications enhanced quantum yield and charge-transfer properties, particularly for sulfur-treated GQDs. When applied to epinephrine sensing, S-GQDs exhibited the most favorable electrochemical performance, enabling detection down to 77 nM. Although this sensitivity is higher than that reported for advanced voltammetric techniques, it is notable for a CV-based sensor and highlights the promise of PLAL-derived GQDs in biosensing.

Beyond analytical performance, these findings emphasize the synergy between material design and green synthesis in electrochemical sensing. By leveraging the eco-friendly, surfactant-free nature of PLAL, this work demonstrates the feasibility of producing high-purity GQDs with tunable surface chemistry and improved electrocatalytic activity. The incorporation of chlorine, together with surface modifications from sulfur and nitrogen treatments, modulated physicochemical properties and enhanced interaction with electrode modifiers and analytes, thereby improving sensor functionality.

Taken together, the results position PLAL-derived GQDs as sustainable and versatile building blocks for electrochemical sensors. Their ability to combine environmentally responsible synthesis with strong performance in biologically and clinically relevant detection opens promising avenues for real-time monitoring and broader applications in environmental and biomedical technologies.

Journal Pre-proof

ASSOCIATED CONTENT

Supporting Information

Supplementary data to this article can be found online at doi:xxxxx

AUTHOR INFORMATION

Corresponding Author

*E-mail: m.fredel@ufsc.br

ORCID

Philipi Cavalcante Ricardo: 0000-0002-2961-2540

Caio Raphael Vanoni: 0000-0003-2946-168X

Jorge Padrão (J. P.): 0000-0001-5630-6621

Andrea Zille (A. Z.): 0000-0001-5299-4164

Veronica Satulu (V. S.): 0000-0003-4073-3041

Bogdana Mitu (B. M.): 0000-0002-0603-4864

Mario Rui Pereira (M.R.P.): 0000-0002-3751-0552

Cristiane Luisa Jost (C. L. J.): 0000-0001-6213-1928

Filipe Samuel Silva (F. S. S.): 0000-0003-3596-3328

Márcio Celso Fredel (M. C. F.): 0000-0001-7020-762X

Present Addresses

P.C.R.: Ceramic and Composite Materials Research Group (CERMAT), Mechanical Engineering Department, Federal University of Santa Catarina, Florianópolis SC, Brazil;

C.R.V.: ampere - Laboratório de Plataformas Eletroquímicas, Department of Chemistry, Federal University of Santa Catarina – UFSC, Florianópolis, SC 88040-900, Brazil;

Journal Pre-proof

J. P.: Centre for Textile Science and Technology (2C2T), University of Minho, 4800-058 Guimarães, Portugal;

V.S.: Low Temperature Plasma Physics Department, National Institute for Laser, Plasma and Radiation Physics, Magurele, Romania.

B.M.: Innovation Centre in Photonics and Plasma for Advanced Materials and Technologies, National Institute for Laser, Plasma and Radiation Physics, Magurele, Romania.

M. R. P.: Centre of Physics of University of Minho and Porto (CF-UM-UP), Campus de Gualtar, 4710-057 Braga, Portugal

C. L. J.: ampere – Electrochemical Platforms Laboratory, Department of Chemistry, Federal University of Santa Catarina – UFSC, Florianópolis, SC 88040-900, Brazil;

F. S. S.: Center for Micro Electro Mechanical Systems (CMEMS), University of Minho, 4800-058 Guimarães, Portugal;

M.C.F.: Ceramic and Composite Materials Research Group (CERMAT), Mechanical Engineering Department, Federal University of Santa Catarina, Florianópolis SC, Brazil.

Author Contributions

P.C.R.: Conceptualization, Methodology, Investigation, Data curation, Formal analysis, Writing – Original draft;

C.R.V.: Methodology, Investigation, Data curation, Formal analysis, Writing – Original draft;

J. P.: Writing – review & editing;

A. Z.: Writing – review & editing;

V. S.: Methodology, Investigation, viewing.

Journal Pre-proof

B.M.: Methodology, Data curation, Writing -review and editing;

M.R.P.: Methodology, Investigation, Writing – review & editing;

C. L. J.: Methodology, Investigation, Resources, Funding acquisition, Writing – review & editing;

F.S.S.: Supervision, Resources, Funding acquisition, Project administration, Writing – review & editing;

M.C.F.: Supervision, Validation, Resources, Funding acquisition, Project administration, Writing – review & editing.

Notes

The authors declare no competing financial interest.

ACKNOWLEDGMENTS

This study was supported by CNPq (Conselho Nacional de Desenvolvimento Científico e Tecnológico, grants 409269/2023-9 and 403757/2024-0), which also provided scholarships and fellowships to the authors (P.C.R. and C.R.V.). C.L.J. acknowledges funding from Fundação de Apoio à Pesquisa e Inovação do Estado de Santa Catarina – FAPESC (03/2022 2022TR001391). This study was also financed in part by the Coordenação de Aperfeiçoamento de Pessoal de Nível Superior – Brasil (CAPES) – Finance Code 001. Funding was also provided by the European Regional Development Fund through the Operational Competitiveness Program and the National Foundation for Science and Technology of Portugal (FCT) under the projects UID/CTM/00264/2020 of the Centre for Textile Science and Technology (2C2T) and its base (DOI: 10.54499/UIDB/00264/2020, accessed on 5 May 2025) and programmatic (DOI: 10.54499/UIDP/00264/2020) components. V.S. And B.M. acknowledge the financial support of the Romanian Ministry of Education and Research through Nucleus programme, Project

Journal Pre-proof

LAPLAS VI – ctr 30 N/2023. The authors acknowledge Rafael Santiago Floriani Pereira for his contribution to the laser interferometry analysis.

DATA AVAILABILITY

The authors confirm that the data supporting the findings of this study are included within the article and its Supporting Information. Furthermore, raw data that underpin the results of this study are available from the corresponding author upon reasonable request.

Journal Pre-proof

5. REFERENCES

[1] G. Bae, H. Cho, B.H. Hong, A review on synthesis, properties, and biomedical applications of graphene quantum dots (GQDs), Nanotechnology 35 (2024) 372001. https://doi.org/10.1088/1361-6528/AD55D0.

[2] S. Lai, Y. Jin, L. Shi, R. Zhou, Y. Li, Fluorescence Sensing Mechanisms of Versatile Graphene Quantum Dots toward Commonly Encountered Heavy Metal Ions, ACS Sensors 8 (2023) 3812–3823. https://doi.org/10.1021/acssensors.3c01295.

[3] A. Ghaffarkhah, E. Hosseini, M. Kamkar, A.A. Sehat, S. Dordanihaghighi, A. Allahbakhsh, C. van der Kuur, M. Arjmand, Synthesis, Applications, and Prospects of Graphene Quantum Dots: A Comprehensive Review, Small 18 (2022) 2102683. https://doi.org/10.1002/SMLL.202102683.

[4] Y. Huang, D. Wang, Y. Wei, X. Dong, R. Yang, H. Li, M. Wei, J. Yu, L. Zhong, Y. Xu, Advances in synthesis of the graphene quantum dots from varied raw materials, Arab. J. Chem. 17 (2024) 105533. https://doi.org/10.1016/J.ARABJC.2023.105533.

[5] B. Mahto, B. Mahanty, S. Hait, S. Hussain, A review of coal-based carbon and graphene quantum dots: synthesis, properties, and applications, Mater. Sci. Eng. B 304 (2024) 117386. https://doi.org/10.1016/J.MSEB.2024.117386.

[6] T. Zhao, K. Wang, F. Liu, S. Zhang, S.-H. Ho, Recent progress of tailoring valuable graphene quantum dots from biomass, Chinese Chem. Lett. 36 (2025) 110321. https://doi.org/10.1016/J.CCLET.2024.110321.

[7] L. Ruiyi, Z. Huahua, L. Zaijun, Switchable two-color graphene quantum dot as a promising fluorescence probe to highly sensitive pH detection and bioimaging, Spectrochim. Acta Part A Mol. Biomol. Spectrosc. 275 (2022) 121028. https://doi.org/10.1016/j.saa.2022.121028.

Journal Pre-proof

[8] M.H. Karami, M. Abdouss, A. Rahdar, S. Pandey, Graphene quantum dots: Background, synthesis methods, and applications as nanocarrier in drug delivery and cancer treatment: An updated review, Inorg. Chem. Commun. 161 (2024) 112032. https://doi.org/10.1016/J.INOCHE.2024.112032.

[9] D. Liu, H.J. Li, B. Lyu, S. Cheng, Y. Zhu, P. Wang, D. Wang, X. Wang, J. Yang, Efficient performance enhancement of GaN-based vertical light-emitting diodes coated with N-doped graphene quantum dots, Opt. Mater. (Amst). 89 (2019) 468–472. https://doi.org/10.1016/J.OPTMAT.2019.01.026.

[10] M. Panachikkool, T. Pandiyarajan, Graphene quantum dots as game-changers in solar cell technology: a review of synthetic processes and performance enhancement, Carbon Lett. 2023 341 34 (2023) 445–475. https://doi.org/10.1007/S42823-023-00617-W.

[11] A.R.S. Lima, A. Mikhraliieva, C.R. Vanoni, M. Nazarkovsky, Y. Xing, M.T. Couto, V. Zaitsev, C.L. Jost, 2D-network of boron-functionalized N-doped graphene quantum dots for electrochemical sensing of dopamine, Diam. Relat. Mater. 146 (2024) 111259. https://doi.org/10.1016/j.diamond.2024.111259.

[12] R. Wu, Y. Cao, Z. Chen, J.-J. Zhu, Fluorescent graphene quantum dots: Properties regulation, sensing applications, and future prospects, Adv. Sens. Energy Mater. 4 (2025) 100140. https://doi.org/10.1016/J.ASEMS.2025.100140.

[13] Z. Ouyang, Y. Lei, L. Luo, al -, G. Bae, H. Cho, B. Hee Hong -, L. Golubewa, T. Kulahava, A. Klimovich, F. Sun, H. Ghosh, Z. Tan, S. Sivoththaman, Top-down synthesis and enhancing device adaptability of graphene quantum dots, Nanotechnology 34 (2023) 185601. https://doi.org/10.1088/1361-6528/ACB7FB.

[14] M.H.M. Facure, R. Schneider, L.A. Mercante, D.S. Correa, Rational hydrothermal synthesis of graphene quantum dots with optimized luminescent properties for sensing

applications, Mater. Today Chem. 23 (2022) 100755. https://doi.org/10.1016/j.mtchem.2021.100755.

[15] N. Sohal, S. Singla, S.J. Malode, S. Basu, B. Maity, N.P. Shetti, Bioresource-Based Graphene Quantum Dots and Their Applications: A Review, ACS Appl. Nano Mater. 6 (2023) 10925–10943. https://doi.org/10.1021/ACSANM.3C02185/ASSET/IMAGES/LARGE/AN3C02185_0012.JPEG.

[16] D. Huang, H. Zhou, Y. Wu, T. Wang, L. Sun, P. Gao, Y. Sun, H. Huang, G. Zhou, J. Hu, Bottom-up synthesis and structural design strategy for graphene quantum dots with tunable emission to the near infrared region, Carbon N. Y. 142 (2019) 673–684. https://doi.org/10.1016/j.carbon.2018.10.047.

[17] Z. Liu, S. Fu, X. Liu, A. Narita, P. Samorì, M. Bonn, H.I. Wang, Z. Liu, P. Samorì, S. Fu, X. Liu, A. Narita, M. Bonn, H.I. Wang, Small Size, Big Impact: Recent Progress in Bottom-Up Synthesized Nanographenes for Optoelectronic and Energy Applications, Adv. Sci. 9 (2022) 2106055. https://doi.org/10.1002/ADVS.202106055.

[18] L. Shi, B. Wang, S. Lu, Efficient bottom-up synthesis of graphene quantum dots at an atomically precise level, Matter 6 (2023) 728–760. https://doi.org/10.1016/J.MATT.2023.01.003.

[19] R.S. Juang, C. Te Hsieh, C.P. Kao, Y.A. Gandomi, C.C. Fu, S.H. Liu, S. Gu, Highly fluorescent green and red emissions from boron-doped graphene quantum dots under blue light illumination, Carbon N. Y. 176 (2021) 61–70. https://doi.org/10.1016/J.CARBON.2021.01.019.

[20] J. Yang, P. Li, Z. Song, J. Li, H. Yang, F. Yan, L. Li, C. Xu, J. Chen, L. Chen, Graphene quantum dots via ion modification for improving photoluminescence stability in aqueous

Journal Pre-proof

solution with heavy metal ions, Appl. Surf. Sci. 593 (2022) 153367. https://doi.org/10.1016/J.APSUSC.2022.153367.

[21] A. Raghavan, M. Radhakrishnan, K. Soren, P. Wadnerkar, A. Kumar, S. Chakravarty, S. Ghosh, Biological Evaluation of Graphene Quantum Dots and Nitrogen-Doped Graphene Quantum Dots as Neurotrophic Agents, ACS Appl. Bio Mater. 6 (2023) 2237–2247. https://doi.org/10.1021/ACSABM.3C00099/ASSET/IMAGES/LARGE/MT3C00099_0010.JPEG.

[22] N. Buatong, C. Ruttanapun, C. Sriwong, Synthesis of reduced graphene oxide quantum dots from graphene oxide via hydrothermal process and theirs structural, luminescence and magnetic properties, J. Taiwan Inst. Chem. Eng. 142 (2023) 104667. https://doi.org/10.1016/J.JTICE.2022.104667.

[23] A. Aygun, I. Cobas, R.N.E. Tiri, F. Sen, Hydrothermal synthesis of B, S, and N-doped carbon quantum dots for colorimetric sensing of heavy metal ions, RSC Adv. 14 (2024) 10814–10825. https://doi.org/10.1039/D4RA00397G.

[24] Y. Zhu, L. Yan, M. Xu, Y. Li, X. Song, L. Yin, Difference between ammonia and urea on nitrogen doping of graphene quantum dots, Colloids Surfaces A Physicochem. Eng. Asp. 610 (2021) 125703. https://doi.org/10.1016/J.COLSURFA.2020.125703.

[25] L. Shen, X. Chen, Y. Chen, J. Peng, A. Abbas, J. Wei, C. Yu, J. Li, Y. Li, One-Step Hydrothermal Synthesis of Sulfur Quantum Dots for Photoelectrochemical Catalysis for Dye Degradation, J. Electron. Mater. 51 (2022) 3092–3100. https://doi.org/10.1007/S11664-022-09528-4/FIGURES/7.

[26] W. Wang, S. Xu, N. Li, Z. Huang, B. Su, X. Chen, Sulfur and phosphorus co-doped graphene quantum dots for fluorescent monitoring of nitrite in pickles, Spectrochim. Acta Part A Mol. Biomol. Spectrosc. 221 (2019) 117211.

https://doi.org/10.1016/J.SAA.2019.117211.

[27] O. Slezak, M. Kalal, H. Jin Kong -, K.J. Stevenson, E. Romadina, N. Akhmetov, al -, C. Xie, C. Ma, C. Wang, S. Deeksha Dsouza, M. Buerkle, B. Alessi, P. Brunet, A. Morelli, A. Farokh Payam, P. Maguire, D. Mariotti, V. Svrcek, Synthesis of water-stable and highly luminescent graphite quantum dots, Nanotechnology 34 (2023) 505601. https://doi.org/10.1088/1361-6528/ACF7CC.

[28] D. Mombrú, M. Romero, R. Faccio, Á.W. Mombrú, Electronic and optical properties of sulfur and nitrogen doped graphene quantum dots: A theoretical study, Phys. E Low-Dimensional Syst. Nanostructures 113 (2019) 130–136. https://doi.org/10.1016/J.PHYSE.2019.05.004.

[29] X. Hai, Q.X. Mao, W.J. Wang, X.F. Wang, X.W. Chen, J.H. Wang, An acid-free microwave approach to prepare highly luminescent boron-doped graphene quantum dots for cell imaging, J. Mater. Chem. B 3 (2015) 9109–9114. https://doi.org/10.1039/C5TB01954K.

[30] G. Yang, C. Wu, X. Luo, X. Liu, Y. Gao, P. Wu, C. Cai, S. Scott Saavedra, Exploring the Emissive States of Heteroatom-Doped Graphene Quantum Dots, J. Phys. Chem. C 122 (2018) 6483–6492. https://doi.org/10.1021/ACS.JPCC.8B01385/ASSET/IMAGES/LARGE/JP-2018-01385R_0006.JPEG.

[31] Y. Li, S. Li, Y. Wang, J. Wang, H. Liu, X. Liu, L. Wang, X. Liu, W. Xue, N. Ma, Electrochemical synthesis of phosphorus-doped graphene quantum dots for free radical scavenging, Phys. Chem. Chem. Phys. 19 (2017) 11631–11638. https://doi.org/10.1039/C6CP06377B.

[32] M.A.C. de Oliveira, M. Brunet Cabré, C. Schröder, H. Nolan, F. Pota, J.A. Behan, F.

Journal Pre-proof

Barrière, K. McKelvey, P.E. Colavita, Single-Entity Electrochemistry of N-Doped Graphene Oxide Nanostructures for Improved Kinetics of Vanadyl Oxidation, Small 21 (2024) 2405220. https://doi.org/10.1002/SMLL.202405220;REQUESTEDJOURNAL:JOURNAL:16136829;WGROUP:STRING:PUBLICATION.

[33] N. Sohal, B. Maity, S. Basu, Recent advances in heteroatom-doped graphene quantum dots for sensing applications, RSC Adv. 11 (2021) 25586–25615. https://doi.org/10.1039/d1ra04248c.

[34] N. Nesakumar, S. Srinivasan, S. Alwarappan, Graphene quantum dots: synthesis, properties, and applications to the development of optical and electrochemical sensors for chemical sensing, Springer Vienna, 2022. https://doi.org/10.1007/s00604-022-05353-y.

[35] P.C. Ricardo, G. Nicolodelli, M.C. Fredel, P. Cavalcante, G. Nicolodelli, P.C. Ricardo, G. Nicolodelli, M.C. Fredel, Tunable photoluminescence of graphene quantum dots synthesized via laser ablation in ethanol, J. Lumin. 281 (2025) 121186. https://doi.org/10.1016/J.JLUMIN.2025.121186.

[36] M. Alhajj, S.K. Ghoshal, Sustainability, safety, biocompatibility and benefits of laser ablated gold, silver and copper nanoparticles: A comprehensive review, J. Mol. Liq. 414 (2024) 126130. https://doi.org/10.1016/J.MOLLIQ.2024.126130.

[37] I.Y. Khairani, G. Mínguez-Vega, C. Doñate-Buendía, B. Gökce, Green nanoparticle synthesis at scale: a perspective on overcoming the limits of pulsed laser ablation in liquids for high-throughput production, Phys. Chem. Chem. Phys. 25 (2023) 19380–19408. https://doi.org/10.1039/D3CP01214J.

[38] M. Spellauge, C. Doñate-Buendía, S. Barcikowski, B. Gökce, H.P. Huber, Comparison of ultrashort pulse ablation of gold in air and water by time-resolved experiments, Light Sci.

Appl. 11 (2022). https://doi.org/10.1038/s41377-022-00751-6.

[39] D.C. Costa, M. Fernandes, C. Moura, G. Miranda, F. Silva, Ó. Carvalho, S. Madeira, Laser ablation in liquid-assisted synthesis of three types of nanoparticles for enhanced antibacterial applications, Int. J. Precis. Eng. Manuf. - Green Technol. (2025) 1–19. https://doi.org/10.1007/S40684-025-00711-6/METRICS.

[40] I.Y. Khairani, G. Mínguez-Vega, C. Doñate-Buendía, B. Gökce, Green nanoparticle synthesis at scale: a perspective on overcoming the limits of pulsed laser ablation in liquids for high-throughput production, Phys. Chem. Chem. Phys. 25 (2023) 19380–19408. https://doi.org/10.1039/d3cp01214j.

[41] A. Subhan, A.H.I. Mourad, Y. Al-Douri, Influence of Laser Process Parameters, Liquid Medium, and External Field on the Synthesis of Colloidal Metal Nanoparticles Using Pulsed Laser Ablation in Liquid: A Review, Nanomaterials 12 (2022). https://doi.org/10.3390/nano12132144.

[42] I.C. Amaechi, I. Asuo, I. Ka, R. Nechache, A. Pignolet, Stability Enhancement of Perovskite-Based Indoor Photovoltaics with Pulsed Laser-Ablated 2D-Layered Nanomaterials, ACS Appl. Energy Mater. 7 (2024) 12155–12164. https://doi.org/10.1021/ACSAEM.4C02890/ASSET/IMAGES/LARGE/AE4C02890_0006.JPEG.

[43] C. Hamelink, O. Tjurmina, R. Damadzic, W.S. Young, E. Weihe, H.W. Lee, L.E. Eiden, Pituitary adenylate cyclase-activating polypeptide is a sympathoadrenal neurotransmitter involved in catecholamine regulation and glucohomeostasis, Proc. Natl. Acad. Sci. U. S. A. 99 (2002) 461–466. https://doi.org/10.1073/PNAS.012608999.

[44] J. Motiejunaite, L. Amar, E. Vidal-Petiot, Adrenergic receptors and cardiovascular effects of catecholamines, Ann. Endocrinol. (Paris). 82 (2021) 193–197.

Journal Pre-proof

https://doi.org/10.1016/J.ANDO.2020.03.012.

[45] E. Wierzbicka, M. Szultka-Młyńska, B. Buszewski, G.D. Sulka, Epinephrine sensing at nanostructured Au electrode and determination its oxidative metabolism, Sensors Actuators B Chem. 237 (2016) 206–215. https://doi.org/10.1016/J.SNB.2016.06.073.

[46] K.M. Oltmanns, H. Gehring, S. Rudolf, B. Schultes, S. Rook, U. Schweiger, J. Born, H.L. Fehm, A. Peters, Hypoxia causes glucose intolerance in humans, Am. J. Respir. Crit. Care Med. 169 (2004) 1231–1237. https://doi.org/10.1164/RCCM.200308-1200OC/SUPPL_FILE/REVONLINE_DATA_SUPPLEMENT_200308-1200OC.R1.PDF.

[47] T.E. Dribin, S. Waserman, P.J. Turner, Who Needs Epinephrine? Anaphylaxis, Autoinjectors, and Parachutes, J. Allergy Clin. Immunol. Pract. 11 (2023) 1036–1046. https://doi.org/10.1016/J.JAIP.2023.02.002.

[48] Y. Yao, R. Shen, J. Xu, Z. Feng, Progress in electrochemical sensing of epinephrine using carbon nanomaterials: A review, Int. J. Electrochem. Sci. 19 (2024) 100750. https://doi.org/10.1016/J.IJOES.2024.100750.

[49] S. Govindaraju, A.S. Reddy, J. Kim, K. Yun, Sensitive detection of epinephrine in human serum via fluorescence enhancement of gold nanoclusters, Appl. Surf. Sci. 498 (2019) 143837. https://doi.org/10.1016/J.APSUSC.2019.143837.

[50] S. Kongkiatpaiboon, N. Duangdee, S. Chewchinda, O. Poachanukoon, K. Amnuaypattanapon, Development and validation of stability indicating HPLC method for determination of adrenaline tartrate, J. King Saud Univ. - Sci. 31 (2019) 48–51. https://doi.org/10.1016/J.JKSUS.2017.05.016.

[51] A.M. Cohen, L. Wiseman, A. Al Faraj, P. Andreou, R. Hall, V.M. Neira, Use of a liquid chromatography-tandem mass spectrometry method to assess the concentration of epinephrine, norepinephrine, and phenylephrine stored in plastic syringes, Pharm. Technol.

Hosp. Pharm. 8 (2023). https://doi.org/10.1515/PTHP-2022-0010.

[52] A. Dowek, M. Berge, P. Prognon, F.X. Legrand, E. Larquet, A. Tfayli, L.M.M. Lê, E. Caudron, Discriminative and quantitative analysis of norepinephrine and epinephrine by surface-enhanced Raman spectroscopy with gold nanoparticle suspensions, Anal. Bioanal. Chem. 414 (2022) 1163–1176. https://doi.org/10.1007/S00216-021-03743-4/FIGURES/10.

[53] H.A. Asmaa, T.N. Al-Sabha, S.M.J. Al-Mtwaiti, Spectrophotometric Determination of Adrenaline, Phenylephrine Hydrochloride, and Terbutaline Sulfate Using the Gibbs Reagent, J. Anal. Chem. 79 (2024) 784–797. https://doi.org/10.1134/S1061934824700163/FIGURES/7.

[54] T. Li, Z. Wang, H. Xie, Z. Fu, Highly sensitive trivalent copper chelate-luminol chemiluminescence system for capillary electrophoresis detection of epinephrine in the urine of smoker, J. Chromatogr. B 911 (2012) 1–5. https://doi.org/10.1016/J.JCHROMB.2012.10.017.

[55] J. Baranwal, B. Barse, G. Gatto, G. Broncova, A. Kumar, Electrochemical Sensors and Their Applications: A Review, 10 (2022) 363. https://doi.org/10.3390/CHEMOSENSORS10090363.

[56] R.M.F. Baptista, B. Silva, J. Oliveira, V.B. Isfahani, B. Almeida, M.R. Pereira, N. Cerca, C. Castro, P. V. Rodrigues, A. Machado, M. Belsley, E. de M. Gomes, High Piezoelectric Output Voltage from Blue Fluorescent N,N-Dimethyl-4-nitroaniline Nano Crystals in Poly-L-Lactic Acid Electrospun Fibers, Materials (Basel). 15 (2022) 7958. https://doi.org/10.3390/MA15227958/S1.

[57] R.L. Calabro, D.S. Yang, D.Y. Kim, Controlled Nitrogen Doping of Graphene Quantum Dots through Laser Ablation in Aqueous Solutions for Photoluminescence and

Journal Pre-proof

Electrocatalytic Applications, ACS Appl. Nano Mater. 2 (2019) 6948–6959. https://doi.org/10.1021/acsanm.9b01433.

[58] S. Kang, H. Han, K. Lee, K.M. Kim, Ultrasensitive Detection of Fe3+Ions Using Functionalized Graphene Quantum Dots Fabricated by a One-Step Pulsed Laser Ablation Process, ACS Omega 7 (2022) 2074–2081. https://doi.org/10.1021/acsomega.1c05542.

[59] A.P. de M. Rocha, M.I. Alayo, D.M. da Silva, Synthesis of Nitrogen-Doped Graphene Quantum Dots from Sucrose Carbonization, Appl. Sci. 12 (2022). https://doi.org/10.3390/APP12178686.

[60] A.M. Mahmoud, M.H. Mahnashi, S.A. Alkahtani, M.M. El-Wekil, Nitrogen and sulfur co-doped graphene quantum dots/nanocellulose nanohybrid for electrochemical sensing of anti-schizophrenic drug olanzapine in pharmaceuticals and human biological fluids., Int. J. Biol. Macromol. 165 (2020) 2030–2037. https://doi.org/10.1016/J.IJBIOMAC.2020.10.084.

[61] F. Akhgari, N. Samadi, K. Farhadi, M. Akhgari, A green one-pot synthesis of nitrogen and sulfur co-doped carbon quantum dots for sensitive and selective detection of cephalexin, Can. J. Chem. 95 (2017) 641–648. https://doi.org/10.1139/CJC-2016-0531.

[62] H. Safardoust-Hojaghan, O. Amiri, M. Hassanpour, M. Panahi-Kalamuei, H. Moayedi, M. Salavati-Niasari, S,N co-doped graphene quantum dots-induced ascorbic acid fluorescent sensor: Design, characterization and performance, Food Chem. 295 (2019) 530–536. https://doi.org/10.1016/j.foodchem.2019.05.169.

[63] J. Ye, S. Luo, A. Huang, J. Chen, C. Liu, D.J. McClements, Synthesis and characterization of citric acid esterified rice starch by reactive extrusion: A new method of producing resistant starch, Food Hydrocoll. 92 (2019) 135–142. https://doi.org/10.1016/j.foodhyd.2019.01.064.

Journal Pre-proof

[64] H. Kuzhandaivel, S. Manickam, S.K. Balasingam, M.C. Franklin, H.J. Kim, K.S. Nallathambi, Sulfur and nitrogen-doped graphene quantum dots/PANI nanocomposites for supercapacitors, New J. Chem. 45 (2021) 4101–4110. https://doi.org/10.1039/D1NJ00038A.

[65] J. Zhao, L. Tang, J. Xiang, R. Ji, J. Yuan, J. Zhao, R. Yu, Y. Tai, L. Song, Chlorine doped graphene quantum dots: Preparation, properties, and photovoltaic detectors, Appl. Phys. Lett. 105 (2014). https://doi.org/10.1063/1.4896278/132921.

[66] J. Zhao, L. Tang, J. Xiang, R. Ji, Y. Hu, J. Yuan, J. Zhao, Y. Tai, Y. Cai, Fabrication and properties of a high-performance chlorine doped graphene quantum dot based photovoltaic detector, RSC Adv. 5 (2015) 29222–29229. https://doi.org/10.1039/C5RA02358K.

[67] H.S. Rady, M.H. Misbah, M. El-Kemary, Gram-scale synthesis of highly doped chlorine graphene quantum dots: Synthesis and photoluminescence properties, Carbon N. Y. 214 (2023) 118341. https://doi.org/10.1016/J.CARBON.2023.118341.

[68] S. Kang, S. Kang, Y.K. Jeong, Y.K. Jeong, K.H. Jung, Y. Son, W.R. Kim, J.H. Ryu, J.H. Ryu, K.M. Kim, K.M. Kim, One-step synthesis of sulfur-incorporated graphene quantum dots using pulsed laser ablation for enhancing optical properties, Opt. Express, Vol. 28, Issue 15, Pp. 21659-21667 28 (2020) 21659–21667. https://doi.org/10.1364/OE.398124.

[69] R.L. Calabro, D.S. Yang, D.Y. Kim, Liquid-phase laser ablation synthesis of graphene quantum dots from carbon nano-onions: Comparison with chemical oxidation, J. Colloid Interface Sci. 527 (2018) 132–140. https://doi.org/10.1016/j.jcis.2018.04.113.

[70] L. Wang, Y. Li, Y. Wang, W. Kong, Q. Lu, X. Liu, D. Zhang, L. Qu, Chlorine-Doped Graphene Quantum Dots with Enhanced Anti- and Pro-Oxidant Properties, ACS Appl. Mater. Interfaces 11 (2019) 21822–21829. https://doi.org/10.1021/ACSAMI.9B03194/ASSET/IMAGES/LARGE/AM-2019-

03194Q_0007.JPEG.

[71] I.C. Novoa-De León, J. Johny, S. Vázquez-Rodríguez, N. García-Gómez, S. Carranza-Bernal, I. Mendivil, S. Shaji, S. Sepúlveda-Guzmán, Tuning the luminescence of nitrogen-doped graphene quantum dots synthesized by pulsed laser ablation in liquid and their use as a selective photoluminescence on–off–on probe for ascorbic acid detection, Carbon N. Y. 150 (2019) 455–464. https://doi.org/10.1016/j.carbon.2019.05.057.

[72] Z. Ouyang, Y. Lei, L. Luo, al -, W. Zhang, J. Dong, K. Wang, P.R. Kharangarh, S. Umapathy, G. Singh -, S. Kadian, G. Manik, A. Kalkal, M. Singh, R. Pal Chauhan, R.P. Chauhan, Z. Ouyang, Y. Lei, L. Luo, al -, W. Zhang, J. Dong, K. Wang, P.R. Kharangarh, S. Umapathy, G. Singh -, S. Kadian, G. Manik, A. Kalkal, M. Singh, R. Pal Chauhan, Effect of sulfur doping on fluorescence and quantum yield of graphene quantum dots: an experimental and theoretical investigation, Nanotechnology 30 (2019) 435704. https://doi.org/10.1088/1361-6528/AB3566.

[73] D. Ozyurt, S. Shafqat, T.T. Pakkanen, R.K. Hocking, A. Mouritz, B. Fox, Aggregation induced emission transformation of liquid and solid-state N-doped graphene quantum dots, Carbon N. Y. 175 (2021) 576–584. https://doi.org/10.1016/j.carbon.2021.01.026.

[74] Y. Luo, M. Li, L. Sun, Y. Xu, M. Li, G. Hu, T. Tang, J. Wen, X. Li, J. Zhang, L. Wang, High fluorescent sulfur regulating graphene quantum dots with tunable photoluminescence properties, J. Colloid Interface Sci. 529 (2018) 205–213. https://doi.org/10.1016/J.JCIS.2018.06.016.

[75] Z. Gan, H. Xu, Y. Hao, Mechanism for excitation-dependent photoluminescence from graphene quantum dots and other graphene oxide derivates: Consensus, debates and challenges, Nanoscale 8 (2016) 7794–7807. https://doi.org/10.1039/c6nr00605a.

[76] S.R.M. Santiago, T.N. Lin, C.H. Chang, Y.A. Wong, C.A.J. Lin, C.T. Yuan, J.L. Shen,

Synthesis of N-doped graphene quantum dots by pulsed laser ablation with diethylenetriamine (DETA) and their photoluminescence., Phys. Chem. Chem. Phys. 19 33 (2017) 22395–22400. https://doi.org/10.1039/C7CP03993J.

[77] Z. Ouyang, Y. Lei, L. Luo, W. Yao, J. Ren, J. Mao, L. Shen, S. Zhou, F. Huang, H. Zhou, H. Zhang, S. Wang, S. Zhou, Nitrogen-doped graphene quantum dots synthesized by femtosecond laser ablation in liquid from laser induced graphene, Nanotechnology 33 (2021) 115602. https://doi.org/10.1088/1361-6528/AC4069.

[78] X. Niu, Y. Li, H. Shu, J. Wang, Revealing the underlying absorption and emission mechanism of nitrogen doped graphene quantum dots., Nanoscale 8 46 (2016) 19376–19382. https://doi.org/10.1039/C6NR06447G.

[79] L. Shen, S. Zhou, F. Huang, H. Zhou, H. Zhang, S. Wang, S. Zhou, Nitrogen-doped graphene quantum dots synthesized by femtosecond laser ablation in liquid from laser induced graphene, Nanotechnology 33 (2021) 115602. https://doi.org/10.1088/1361-6528/AC4069.

[80] R.M. Altuwirqi, Graphene Nanostructures by Pulsed Laser Ablation in Liquids: A Review, Materials (Basel). 15 (2022) 5925. https://doi.org/10.3390/ma15175925.

[81] K. Wang, J. Dong, L. Sun, H. Chen, Y. Wang, C. Wang, L. Dong, Effects of elemental doping on the photoluminescence properties of graphene quantum dots, RSC Adv. 6 (2016) 91225–91232. https://doi.org/10.1039/C6RA19673J.

[82] M. Yang, Z. Lian, C. Si, B. Li, Revealing the role of nitrogen dopants in tuning the electronic and optical properties of graphene quantum dots via a TD-DFT study., Phys. Chem. Chem. Phys. 22 (2020) 28230–28237. https://doi.org/10.1039/D0CP04707D.

[83] Noor-Ul-Ain, M.O. Eriksson, S. Schmidt, M. Asghar, P.C. Lin, P.O. Holtz, M. Syväjärvi, G. Reza Yazdi, Tuning the Emission Energy of Chemically Doped Graphene Quantum

Journal Pre-proof

Dots, Nanomaterials 6 (2016). https://doi.org/10.3390/NANO6110198.

[84] X. Qin, Z. Zhan, R. Zhang, K. Chu, Z. Whitworth, Z. Ding, Nitrogen- and sulfur-doped graphene quantum dots for chemiluminescence., Nanoscale 15 (2023) 3864–3871. https://doi.org/10.1039/D2NR07213K.

[85] A. Ayala-Fonseca, G. Ramírez-García, J.D. Mota-Morales, A.D.L. Bugallo, E. De la Rosa, P. Salas, Insights on salting-out triggering aggregation-induced emission in nitrogen-doped graphene quantum dots, Carbon N. Y. 216 (2024). https://doi.org/10.1016/J.CARBON.2023.118601.

[86] K. Wang, J. Dong, L. Sun, H. Chen, Y. Wang, C. Wang, L. Dong, Effects of elemental doping on the photoluminescence properties of graphene quantum dots, RSC Adv. 6 (2016) 91225–91232. https://doi.org/10.1039/c6ra19673j.

[87] S. Kang, Y.K. Jeong, J.H. Ryu, Y. Son, W.R. Kim, B. Lee, K.H. Jung, K.M. Kim, Pulsed laser ablation based synthetic route for nitrogen-doped graphene quantum dots using graphite flakes, Appl. Surf. Sci. 506 (2020) 144998. https://doi.org/10.1016/J.APSUSC.2019.144998.

[88] L. Feng, X.Y. Tang, Y.X. Zhong, Y.W. Liu, X.H. Song, S.L. Deng, S.Y. Xie, J.W. Yan, L.S. Zheng, Ultra-bright alkylated graphene quantum dots, Nanoscale 6 (2014) 12635–12643. https://doi.org/10.1039/C4NR03506B.

[89] W. Huang, X. Li, X. Sun, X. Ding, Y. Feng, Y. Tang, P. Zhou, L. Wang, Q. Zhang, Photoluminescence of graphene quantum dots enhanced by microwave post-treatment, Chem. Eng. J. 405 (2021) 126714. https://doi.org/10.1016/J.CEJ.2020.126714.

[90] S.R.M. Santiago, T.N. Lin, C.T. Yuan, J.L. Shen, H.Y. Huang, C.A.J. Lin, Origin of tunable photoluminescence from graphene quantum dots synthesized: Via pulsed laser ablation, Phys. Chem. Chem. Phys. 18 (2016) 22599–22605.

Journal Pre-proof

https://doi.org/10.1039/c6cp03159e.

[91] S. Maiti, S. Kundu, C.N. Roy, T.K. Das, A. Saha, Synthesis of excitation independent highly luminescent graphene quantum dots through perchloric acid oxidation, Langmuir 33 (2017) 14634–14642. https://doi.org/10.1021/ACS.LANGMUIR.7B02611/ASSET/IMAGES/LARGE/LA-2017-02611H_0010.JPEG.

[92] T. Du, J. She, X. Yang, Y. Zhao, S. Zhou, J. Zhao, Role of functionalization in the fluorescence quantum yield of graphene quantum dots, Appl. Phys. Lett. 122 (2023) 142107. https://doi.org/10.1063/5.0144601 (accessed May 20, 2025).

[93] J. Liu, X. Liu, H. Luo, Y. Gao, One-step preparation of nitrogen-doped and surface-passivated carbon quantum dots with high quantum yield and excellent optical properties, RSC Adv. 4 (2014) 7648–7654. https://doi.org/10.1039/C3RA47577H.

[94] P.T. Nga, N.T.M. Huong, L.X. Hung, D.N. Thuan, N.T. Thanh, Y. Bretonnière, F. Lerouge, A. Roux, J. Laverdant, Radiative and non-radiative transfers in co-doped graphene quantum dots, J. Mater. Sci. 60 (2025) 1982–1993. https://doi.org/10.1007/S10853-024-10589-5.

[95] Q. Xu, Y. Liu, C. Gao, J. Wei, H. Zhou, Y. Chen, C. Dong, T.S. Sreeprasad, N. Li, Z. Xia, Synthesis, mechanistic investigation, and application of photoluminescent sulfur and nitrogen co-doped carbon dots, J. Mater. Chem. C 3 (2015) 9885–9893. https://doi.org/10.1039/C5TC01912E.

[96] H. Ding, J.S. Wei, H.M. Xiong, Nitrogen and sulfur co-doped carbon dots with strong blue luminescence., Nanoscale 6 22 (2014) 13817–23. https://doi.org/10.1039/C4NR04267K.

[97] Q. Xu, Y. Liu, C. Gao, J. Wei, H. Zhou, Y. Chen, C. Dong, T.S. Sreeprasad, N. Li, Z. Xia, Synthesis, mechanistic investigation, and application of photoluminescent sulfur and

nitrogen co-doped carbon dots, J. Mater. Chem. C 3 (2015) 9885–9893. https://doi.org/10.1039/C5TC01912E.

[98] P.C. Ricardo, C.R. Vanoni, A.R.S. Lima, C.L. Jost, J. Padrão, F.S. Silva, M.C. Fredel, Tailored ligand-free gold nanoparticles: Exploring green synthesis in saline media for the electrochemical sensing of serotonin, Electrochim. Acta 532 (2025) 146483. https://doi.org/10.1016/j.electacta.2025.146483.

[99] M. Zhou, L.P. Guo, Y. Hou, X.J. Peng, Immobilization of Nafion-ordered mesoporous carbon on a glassy carbon electrode: Application to the detection of epinephrine, Electrochim. Acta 53 (2008) 4176–4184. https://doi.org/10.1016/J.ELECTACTA.2007.12.077.

[100] Y. Yang, C. Li, L. Yin, M. Liu, Z. Wang, Y. Shu, G. Li, Enhanced charge transfer by gold nanoparticle at DNA modified electrode and its application to label-free DNA detection., ACS Appl. Mater. Interfaces 6 10 (2014) 7579–84. https://doi.org/10.1021/AM500912M.

[101] C.E. Sunday, M. Bilibana, S. Qakala, O. Tovide, K.M. Molapo, G. Fomo, C.O. Ikpo, T. Waryo, G. Mbambisa, B. Mpushe, A. Williams, P.G.L. Baker, S. Vilakazi, R. Tshikhudo, E.I. Iwuoha, Modulation of the matrix effect of nafion on tris(bipyridine) ruthenium(II) electrochemical probes by functionalisation with 4-nitrophenylazo graphene-gold nanocomposite, Electrochim. Acta 128 (2014) 128–137. https://doi.org/10.1016/J.ELECTACTA.2013.12.143.

[102] K.J. Aoki, J. Chen, Y. Liu, B. Jia, Peak potential shift of fast cyclic voltammograms owing to capacitance of redox reactions, J. Electroanal. Chem. 856 (2020) 113609. https://doi.org/10.1016/J.JELECHEM.2019.113609.

[103] H.J. Choi, H. jae Choi, J. Kim, H. Choi, C. Chu, I. La, C.Y. Ahn, H. Shim, O.H. Kim, Y.H. Cho, Comparison on the impact of membrane thickness on the performance of proton

Journal Pre-proof

exchange membrane-based electrochemical devices, Int. J. Hydrogen Energy 119 (2025) 161–172. https://doi.org/10.1016/J.IJHYDENE.2025.03.235.

[104] A. Nishimura, K. Toyoda, Y. Kojima, S. Ito, E. Hu, Numerical Simulation on Impacts of Thickness of Nafion Series Membranes and Relative Humidity on PEMFC Operated at 363 K and 373 K, Energies 2021, Vol. 14, Page 8256 14 (2021) 8256. https://doi.org/10.3390/EN14248256.

[105] E. Antolini, L. Giorgi, A. Pozio, E. Passalacqua, Influence of Nafion loading in the catalyst layer of gas-diffusion electrodes for PEFC, J. Power Sources 77 (1999) 136–142. https://doi.org/10.1016/S0378-7753(98)00186-4.

[106] M.C. Daugherty, S. Gu, D.S. Aaron, B. Chandra Mallick, Y.A. Gandomi, C. Te Hsieh, Decorating sulfur and nitrogen co-doped graphene quantum dots on graphite felt as high-performance electrodes for vanadium redox flow batteries, J. Power Sources 477 (2020). https://doi.org/10.1016/J.JPOWSOUR.2020.228709.

[107] C.E. Sunday, M. Bilibana, S. Qakala, O. Tovide, K.M. Molapo, G. Fomo, C.O. Ikpo, T. Waryo, G. Mbambisa, B. Mpushe, A. Williams, P.G.L. Baker, S. Vilakazi, R. Tshikhudo, E.I. Iwuoha, Modulation of the matrix effect of nafion on tris(bipyridine) ruthenium(II) electrochemical probes by functionalisation with 4-nitrophenylazo graphene-gold nanocomposite, Electrochim. Acta 128 (2014) 128–137. https://doi.org/10.1016/J.ELECTACTA.2013.12.143.

[108] E. Dieterich, S.J. Kinkelin, M. Steimecke, M. Bron, Quantifying the removal of stabilizing thiolates from gold nanoparticles on different carbon supports and the effect on their electrochemical properties, Nanoscale Adv. 4 (2022) 5154–5163. https://doi.org/10.1039/D2NA00561A.

[109] L.S. De Bortoli, C.R. Vanoni, C.L. Jost, D.Z. Mezalira, M.C. Fredel, Stable and ligand-

free gold nanoparticles produced by laser ablation as efficient electrocatalysts for electrochemical sensing of dopamine, J. Electroanal. Chem. 947 (2023) 117744. https://doi.org/10.1016/j.jelechem.2023.117744.

[110] A. Mirzahosseini, T. Pálla, G. Orgován, G. Tóth, B. Noszál, Characterization of the species-specific acid-base equilibria of adrenaline and noradrenaline, J. Pharm. Biomed. Anal. 170 (2019) 215–219. https://doi.org/10.1016/J.JPBA.2019.02.035.

[111] Y. Shih, J.M. Zen, A.S. Kumar, P.Y. Chen, Flow injection analysis of zinc pyrithione in hair care products on a cobalt phthalocyanine modified screen-printed carbon electrode, Talanta 62 (2004) 912–917. https://doi.org/10.1016/J.TALANTA.2003.10.039.

[112] S. Kumar, M. Bhuiya, D.K. Palai, N. Agnihotri, Computational Studies on the Nitrogen-Doped Graphene Quantum Dots as Potential Sensor for Hazardous Gases, J. Electron. Mater. 53 (2024) 3548–3559. https://doi.org/10.1007/S11664-024-11122-9/FIGURES/10.

[113] D. Mombrú, M. Romero, R. Faccio, Á.W. Mombrú, Electronic and optical properties of sulfur and nitrogen doped graphene quantum dots: A theoretical study, Phys. E Low-Dimensional Syst. Nanostructures 113 (2019) 130–136. https://doi.org/10.1016/J.PHYSE.2019.05.004.

[114] A. Kousar, T. Laurila, Insights into electrode-electrolyte adsorption dynamics via double potential step chronocoulometry and cyclic voltammetry, J. Electroanal. Chem. 965 (2024) 118374. https://doi.org/10.1016/J.JELECHEM.2024.118374.

[115] M. Sajid, N. Baig, K. Alhooshani, Chemically modified electrodes for electrochemical detection of dopamine: Challenges and opportunities, TrAC Trends Anal. Chem. 118 (2019) 368–385. https://doi.org/10.1016/J.TRAC.2019.05.042.

[116] M.A.V. Devanathan, Kinetics of multiple-electron-transfer reactions—I. The transfer coefficient, Electrochim. Acta 17 (1972) 1683–1697. https://doi.org/10.1016/0013-

4686(72)85057-6.

[117] G.L. Long, J.D. Winefordner, Limit of Detection: A Closer Look at the IUPAC Definition, Anal. Chem. 55 (1983) 712A-724A. https://doi.org/10.1021/AC00258A001/ASSET/AC00258A001.FP.PNG_V03.

[118] M.S. Al Ja'farawy, D. Thirumalai, J. Lee, H.S. Jung, S.C. Chang, J.H. Yoon, D.H. Kim, Graphene quantum dot nanocomposites: electroanalytical and optical sensor technology perspective, J. Anal. Sci. Technol. 14 (2023) 1–23. https://doi.org/10.1186/S40543-023-00393-2/TABLES/5.

[119] S. Uruc, O. Gorduk, Y. Sahin, Fabrication of nickel oxide/copper cobaltite/graphene quantum dot conductive ink as an electrode material for selective electrochemical detection of epinephrine, J. Alloys Compd. 1010 (2025) 177786. https://doi.org/10.1016/J.JALLCOM.2024.177786.

[120] S.E. Elugoke, O.E. Fayemi, A.S. Adekunle, P.S. Ganesh, S.Y. Kim, E.E. Ebenso, Sensitive and selective neurotransmitter epinephrine detection at a carbon quantum dots/copper oxide nanocomposite, J. Electroanal. Chem. 929 (2023) 117120. https://doi.org/10.1016/J.JELECHEM.2022.117120.

[121] P. Thondaiman, R. Manikandan, C.J. Raj, A.D. Savariraj, S.E. Moulton, B.C. Kim, Boron and nitrogen doped graphene quantum dots on a surface modified Cu mesh for the determination of dopamine and epinephrine, Synth. Met. 278 (2021) 116831. https://doi.org/10.1016/J.SYNTHMET.2021.116831.

[122] J. Tashkhourian, S.F. Nami-Ana, M. Shamsipur, Designing a modified electrode based on graphene quantum dot-chitosan application to electrochemical detection of epinephrine, J. Mol. Liq. 266 (2018) 548–556. https://doi.org/10.1016/J.MOLLIQ.2018.06.093.

[123] V. Vinoth, L.N. Natarajan, R.V. Mangalaraja, H. Valdés, S. Anandan, Simultaneous

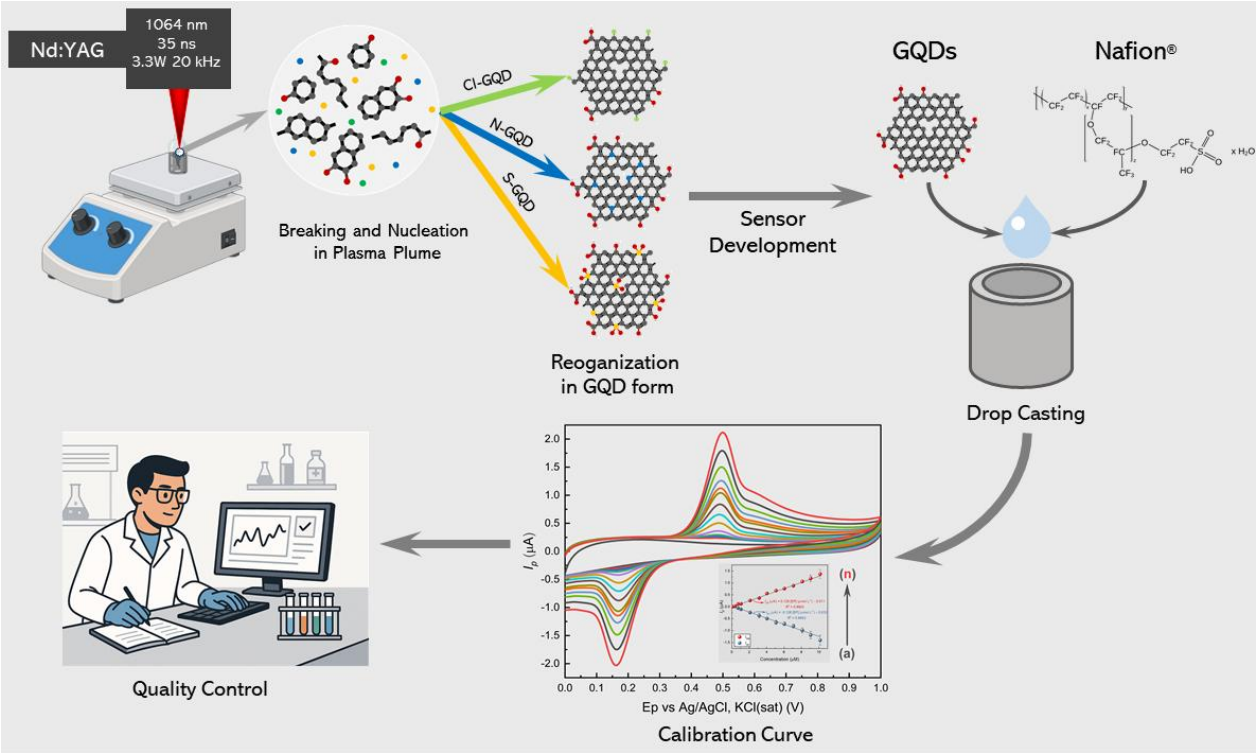
electrochemical determination of dopamine and epinephrine using gold nanocrystals capped with graphene quantum dots in a silica network, Microchim. Acta 186 (2019) 1–12. https://doi.org/10.1007/S00604-019-3779-9/FIGURES/10.

[124] R. S., P. Abraham, V.A. Kumary, P.G. Chithra, K. Sreevalsan, Review—Progress on Carbon-Based Electrochemical Sensors for Epinephrine and Norepinephrine, J. Electrochem. Soc. 169 (2022) 046519. https://doi.org/10.1149/1945-7111/AC5F7E.

[125] E. Oner, S. Uruc, E. Dokur, O. Gorduk, Y. Sahin, Utilization of a Selective Paper-Based Flexible Electrochemical Sensor for Epinephrine Determination in Artificial Sweat Using Nickel Oxide and Sulfur-Doped Graphene Conductive Ink, J. Electrochem. Soc. 172 (2025) 027508. https://doi.org/10.1149/1945-7111/ADB189.

[126] G. Ebube. Uwaya, Y. Wen, K. Bisetty, A combined experimental-computational approach for electrocatalytic detection of epinephrine using nanocomposite sensor based on polyaniline/nickel oxide, J. Electroanal. Chem. 911 (2022) 116204. https://doi.org/10.1016/J.JELECHEM.2022.116204.

Journal Pre-proof



Journal Pre-proof

Declaration of interests

☒The authors declare that they have no known competing financial interests or personal relationships that could have appeared to influence the work reported in this paper.

☐The authors declare the following financial interests/personal relationships which may be considered as potential competing interests:

Journal Pre-proof

Journal Pre-proof

Florianópolis, SC - September 15th, 2025.

Professor Dr. Ken Haenen, PhD

Editor-in-Chief, Diamond and Related Materials

Dear Professor Dr. Ken Haenen,

Please find enclosed the highlights document accompanying the submission of our manuscript, "**Engineering Graphene Quantum Dots via Laser Ablation for Epinephrine Sensing**" for consideration as a research article in **Diamond and Related Materials**.

Highlights:

- Pulsed laser ablation yielded ~4 nm graphene quantum dots in ethanol.
- Na salts tuned surface chemistry via Cl doping and N/S functionalization.
- Quantum yield enhanced from 4.2% (pure) to 8.6% (S-GQDs).
- Nitrogen treatment increased sp^2 carbon fraction to ~72% by XPS analysis.
- GCE/Nafion®/S-GQDs sensor detected epinephrine with 77 nM.

Journal Pre-proof